

Probing the exchange of CO₂ and O₂ in the shallow critical zone during weathering of marl and black shale

Tobias Roylands¹, Robert G. Hilton², Erin L. McClymont¹, Mark H. Garnett³, Guillaume Soulet⁴, Sébastien Klotz⁵, Mathis Degler⁶, Felipe Napoleoni⁷, Caroline Le Bouteiller⁵

5 ¹Department of Geography, Durham University, Durham, DH1 3LE, United Kingdom

²Department of Earth Sciences, University of Oxford, Oxford, OX1 3AN, United Kingdom

³NEIF Radiocarbon Laboratory, SUERC, East Kilbride, G75 0QF, United Kingdom

⁴Ifremer, Geo-Ocean, Brest University, CNRS, Plouzané, 29280, France

⁵INRAE, Univ. Grenoble Alpes, CNRS, Grenoble, 38000, France

10 ⁶Institute of Geosciences, Christian-Albrechts-University, Kiel, 24118, Germany

⁷Centro de Estudios Científicos, Valdivia, 5110466, Chile

Correspondence to: Robert G. Hilton (robert.hilton@earth.ox.ac.uk)

Abstract. Chemical weathering of sedimentary rocks can release carbon dioxide (CO₂) and consume oxygen (O₂) via the oxidation of petrogenic organic carbon and sulfide minerals. These pathways govern Earth's surface system and climate over geological timescales, but the present-day weathering fluxes and their environmental controls are only partly constrained due to a lack of in situ measurements. Here, we investigate the gaseous exchange of CO₂ and O₂ during the oxidative weathering of black shales and marls exposed in the French southern Alps. On six fieldtrips over one year, we use drilled headspace chambers to measure the CO₂ concentrations in the shallow critical zone, and quantify CO₂ fluxes in real-time. Importantly, we develop a new approach to estimate the volume of rock that contributes CO₂ to a chamber, and assess effective diffusive gas exchange, by first quantifying the mass of CO₂ that is stored in a chamber and connected rock pores. Both rock types are characterized by similar contributing rock volumes and diffusive movement of CO₂. However, CO₂ emissions differed between the rock types, with yields over rock outcrop surfaces (inferred from the contributing rock volume and the local weathering depths) ranging on average between 73 tC km⁻² yr⁻¹ and 1,108 tC km⁻² yr⁻¹ for black shales and between 43 tC km⁻² yr⁻¹ and 873 tC km⁻² yr⁻¹ for marls over the study period. Having quantified diffusive processes, chamber-based O₂ concentration measurements are used to calculate O₂ fluxes. The rate of O₂ consumption increased with production of CO₂, and with increased temperature, with an average O₂ : CO₂ molar ratio of 10 : 1. If O₂ consumption occurs by both rock organic carbon oxidation and carbonate dissolution coupled to sulfide oxidation, either an additional O₂ sink needs to be identified, or significant export of dissolved inorganic carbon occurs from the weathering zone. Together, our findings refine the tools we have to probe CO₂ and O₂ exchange in rocks at Earth's surface and shed new light on CO₂ and O₂ fluxes, their drivers and the fate of rock-derived carbon.

1 Introduction

Sedimentary rocks cover ~ 64 % of the present-day continental surface of Earth (Hartmann and Moosdorf, 2012) and contain vast amounts of carbon in carbonate minerals and organic matter (Petsch, 2014). The chemical breakdown of these rocks can act as a source of carbon dioxide (CO₂) to the near-surface reservoirs (hydrosphere-biosphere-pedosphere-atmosphere) and can be a sink of oxygen (O₂), in turn exerting an important control on the evolution of climate and life (Bernier and Bernier, 2012; Bernier, 1999; Sundquist and Visser, 2003). Two reactions are recognized: i) the oxidation of petrogenic organic carbon (OC_{petro}) (Petsch, 2014); and ii) the oxidation of sedimentary sulfide minerals that produce sulfuric acid that can, in turn, dissolve carbonate minerals (Calmels et al., 2007; Li et al., 2008; Torres et al., 2014). On a global scale, these chemical weathering pathways together emit roughly as much CO₂ to the atmosphere (Bernier and Bernier, 2012; Burke et al., 2018; Petsch, 2014) as is removed by the weathering of silicate minerals with a flux of ~ 90 MtC yr⁻¹ – 140 MtC yr⁻¹ (Gaillardet et al., 1999; Moon et al., 2014). How these fluxes play out over longer timescales remains difficult to assess (Petsch, 2014; Hilton and West, 2020), however the decline of atmospheric O₂ over the last 800,000 years (Stolper et al., 2016) has been tentatively linked to changes in global oxidative weathering fluxes (Yan et al., 2021). To improve the understanding of the changes of Earth's surface conditions over geological timescales, the mechanism and controls on oxidative weathering pathways need to be better constrained (Bernier and Bernier, 2012; Mills et al., 2021). Theoretical modeling of OC_{petro} oxidation currently relies on input kinetics of the weathering reactions from laboratory experiments (Bolton et al., 2006; Petsch, 2014; Bao et al., 2017). In situ gas exchange between rocks undergoing weathering and the atmosphere can provide much needed insight.

The first field-based fluxes of weathering-derived CO₂ were reported by Keller and Bacon (1998) in a glacial till dominated by shales. More recently, Tune et al. (2020) found substantial CO₂ release and O₂ depletion in bedrock undergoing weathering below a forested hillslope. There, according to monitoring of gases and water chemistry, carbon release is mostly sourced from superficial soils, deep roots, with minor contributions from OC_{petro} oxidation (Tune et al., 2020, 2023). At both sites, the gaseous fluxes were determined on the basis of profiles of the CO₂ concentration in air sampled from boreholes extending to depths of ~ 7 m (Keller and Bacon, 1998) and of ~ 16 m (Tune et al., 2020), using Fick's law:

$$J_X = -D_X \times \frac{dC_X}{dz}, \quad (1)$$

where J_X is the molar flux (mol m⁻² s⁻¹) of the particular gas species X and D_X its diffusivity (i.e., the capability to allow diffusion, m² s⁻¹) in the studied vadose zone, and where $\frac{dC_X}{dz}$ describes the change of the concentration (mol m⁻³) over depth (m). An alternative approach introduced by Soulet et al. (2018) uses gas accumulation chambers drilled into shallow weathering zones. Instead of calculating a carbon flux from a presupposed diffusion coefficient, which can introduce uncertainties (Maier and Schack-Kirchner, 2014), CO₂ release is measured in real-time in a similar way as commonly applied to soil surfaces (Oertel et al., 2016). This method has provided new insight on how temperature, precipitation and

topography control CO₂ emissions from marls (Soulet et al., 2021) and mudstones (Roylands et al., 2022). However, for weathering chambers that are installed within the rock face, three aspects remain unexplored: i) the rock volume that contributes to the CO₂ accumulation measured in the chamber; ii) how the diffusive movement of CO₂ in the shallow weathering zone is impacted by short-term environmental changes (e.g., in temperature and hydrology); and iii) the quantification of O₂ depletion during oxidative weathering.

In this study, we investigate the weathering-driven exchange of CO₂ and O₂ by installing chambers into black shales and marls undergoing oxidation at two study sites in the steep terrains of the Draix-Bléone observatory, France (Gaillardet et al., 2018; Draix-Bléone Observatory, 2015; Klotz et al., 2023). Building on research from an outcrop at the same observatory (Soulet et al., 2021), we find that chamber-based CO₂ emissions vary significantly over one year, linked to changes in temperature and precipitation. A new theoretical framework is developed to refine CO₂ flux measurements (Sect. 4.1) and applied to quantify the rock pore space that is probed during a measurement (Sect. 4.2). This allows us to normalize CO₂ accumulation rates based on a contributing rock volume, and return estimates of fluxes emitted from the surface of rock outcrops. The resulting CO₂ fluxes can be accurately described as a function of temperature (Sect. 4.3). Using Fick's law, measurements of the O₂ concentration in the chambers are then used to quantify the O₂ consumption in the studied rocks (Sect. 4.4). Together, we provide new insights into the exchange of CO₂ and O₂ in the shallow weathering zone of sedimentary rocks.

2 Material and methods

2.1 Study area

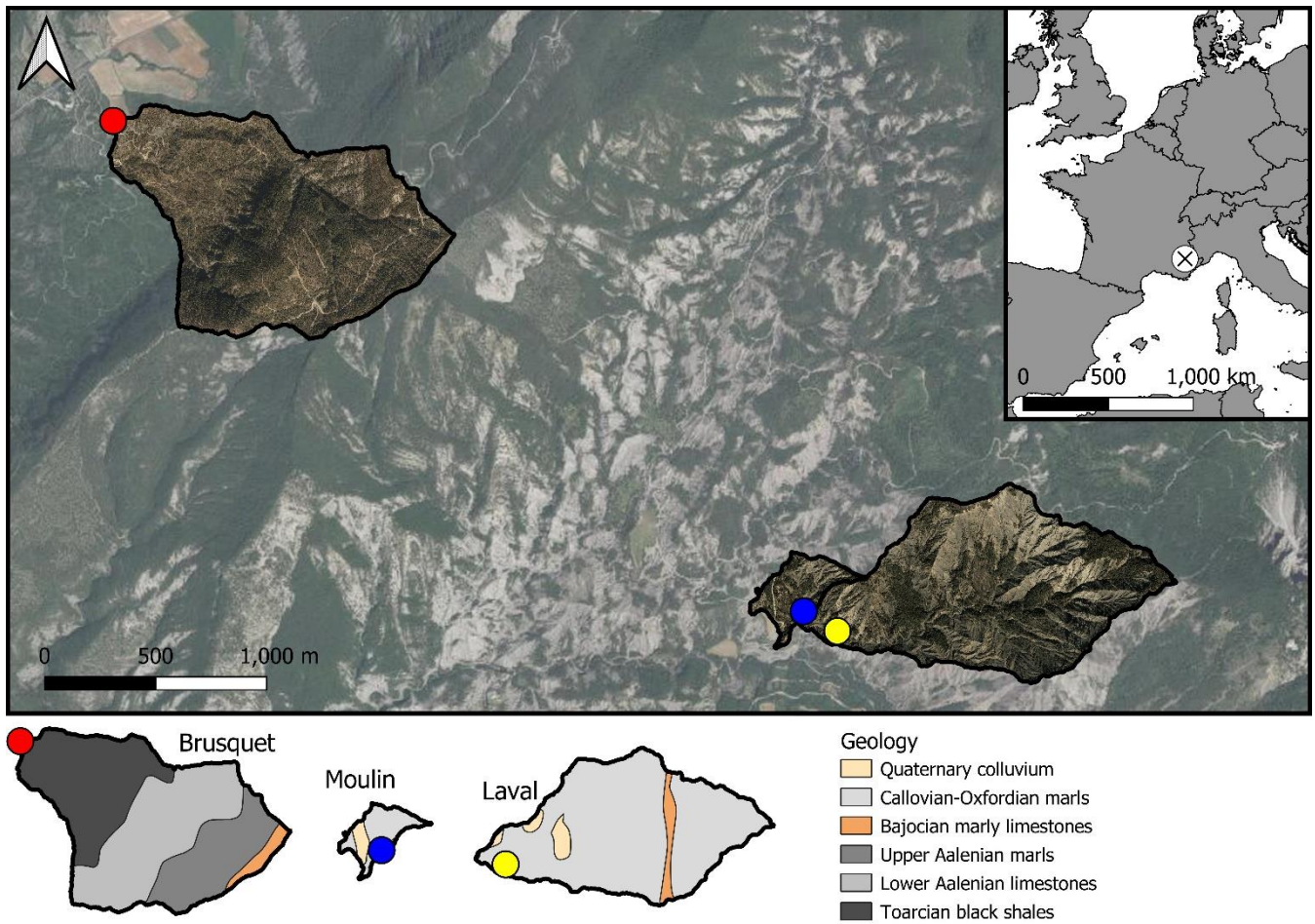
The two study sites are located in the catchments of the Brusquet (area of 1.08 km²) and Moulin (0.08 km²) of the Draix-Bléone observatory (Draix-Bléone Observatory, 2015; Klotz et al., 2023), which is part of the French network of critical zone observatories (OZCAR) (Gaillardet et al., 2018). The Brusquet site is located at 44.16251° N 6.32330° E at 847 m.a.s.l. and the Moulin site at 44.14146° N 6.36095° E at 874 m.a.s.l. (Fig. 1). The catchments of the Draix-Bléone observatory have detailed measurements of river water discharge, river suspended load and bedload transport, and meteorological data over the last 4 decades (Cras et al., 2007; Mathys et al., 2003; Carriere et al., 2020; Draix-Bléone Observatory, 2015; Mathys and Klotz, 2008; Mallet et al., 2020; Klotz et al., 2023). Prior work has examined the occurrence of the solid phase of OC_{petro} in the Brusquet, Moulin and Laval catchments (Graz et al., 2011, 2012; Copard et al., 2006). The Laval catchment (0.86 km²), which neighbors the Moulin catchment (Fig. 1), is the location of previous in situ measurements of rock-derived CO₂ (Soulet et al., 2018, 2021).

The Moulin catchment overlays Callovian to Oxfordian marls (Mathys et al., 2003; Graz et al., 2012; Janjou, 2004). In contrast, the lithology of the Brusquet catchment consists of a sequence of Bajocian marly limestones, Aalenian marls and limestones to Toarcian black shales (Janjou, 2004; Copard et al., 2006; Graz et al., 2011), with the study site located on the latter (Fig. 1).

95 The climate is transitional between Alpine and Mediterranean with a hot and dry summer, including short and intense rainfall events during thunderstorms (up to 150 mm h^{-1}), with rainfall events of lower intensity typically during spring and autumn (Soulet et al., 2021; Carriere et al., 2020; Mathys et al., 2003; Mallet et al., 2020). During winter, more than 100 days of frost can occur (Oostwoud Wijdenes and Ergenzinger, 1998; Rovéra and Robert, 2006) and frost-cracking from ice-segregation was found to control hillslope regolith production (Ariagno et al., 2022). The mean annual rainfall is
100 $\sim 900 \text{ mm}$ and the mean annual air temperature is $\sim 11 \text{ }^\circ\text{C}$ defined by high solar radiation ($> 2,300 \text{ h yr}^{-1}$) (Soulet et al., 2021; Mallet et al., 2020; Mathys and Klotz, 2008).

Together, the climate and the erodible lithology of finely bedded, mechanically weak rocks result in a badland morphology with V-shaped gullies, high physical weathering rates and abrupt, sediment-loaded floods (Antoine et al., 1995; Cras et al., 2007; Le Bouteiller et al., 2021; Mathys et al., 2003). These features limit the development of soils and
105 vegetation cover. In the late 19th century, following overgrazing in the wider area of the observatory, the Brusquet catchment was reforested (Mathys et al., 2003; Cras et al., 2007). Today $\sim 87 \%$ of the catchment area of Brusquet is vegetated, in contrast to $\sim 46 \%$ and $\sim 32 \%$ of the Moulin and Laval catchments, respectively (Carriere et al., 2020; Cras et al., 2007). The sediment export fluxes of the Brusquet catchment are on average $\sim 70 \text{ t km}^{-2} \text{ yr}^{-1}$, and $\sim 5,700 \text{ t km}^{-2} \text{ yr}^{-1}$ and $\sim 14,300 \text{ t km}^{-2} \text{ yr}^{-1}$ for the Moulin and Laval catchments, respectively (Mathys et al., 2003; Carriere et al., 2020). Taking a
110 regolith bulk density of $\sim 1.3 \text{ t m}^{-3}$ - 1.8 t m^{-3} into account (Mallet et al., 2020; Mathys and Klotz, 2008; Oostwoud Wijdenes and Ergenzinger, 1998; Bechet et al., 2016; Ariagno et al., 2023), a physical erosion rate of $\sim 0.04 \text{ mm yr}^{-1}$ - 0.05 mm yr^{-1} , $\sim 3.2 \text{ mm yr}^{-1}$ - 4.4 mm yr^{-1} and $\sim 8 \text{ mm yr}^{-1}$ - 11 mm yr^{-1} can be estimated for the Brusquet, Moulin and Laval catchments, respectively. However, these values are catchment-scale averages, and the physical erosion can significantly vary spatially. On steep, bare slopes, the erosion rates may be comparably high in the different catchments of the Draix-Bléone observatory
115 (Carriere et al., 2020; Bechet et al., 2016; Mathys et al., 2003).

The bare surfaces in the catchments are characterized by four morphologically different layers as reviewed by Mathys and Klotz (2008): i) near surface, loose detrital cover of locally produced clasts or colluvial material with a thickness of ~ 0 - 10 cm ; ii) below, the upper, fine regolith with a thickness of ~ 5 - 20 cm ; and iii) the lower, coarse and compact regolith with a thickness of ~ 10 - 20 cm ; iv) the unweathered bedrock at the bottom (Oostwoud Wijdenes and Ergenzinger,
120 1998; Maquaire et al., 2002; Rovéra and Robert, 2006). The compactness and density of these layers increase, while the porosity decreases (from values of up to $\sim 50 \%$) (Bechet et al., 2016; Mallet et al., 2020; Garel et al., 2012), over depth towards the unweathered bedrock (Maquaire et al., 2002). The unweathered bedrock has a grain density of $\sim 2.7 \text{ t m}^{-3}$ and a porosity of ~ 10 - 20% (Lofi et al., 2012). The thickness of the weathering profile varies laterally with the thickest regolith layers and detrital cover on crests, minimal development in thalwegs and intermediate in gullies (Maquaire et al., 2002;
125 Esteves et al., 2005).



130 **Figure 1:** Location of the French Draix-Bléone observatory and of the study sites for in situ CO₂ and O₂ monitoring in the Brusquet catchment (red circle) and in the Moulin catchment (blue circle), alongside the location of previous research in the Laval catchment for reference (yellow circle) (Soulet et al., 2018, 2021), and geological maps of these catchments (Janjou, 2004). Meteorological stations are present at each of the catchment outlets with a maximum distance to the study sites of 200 m (Draix-Bléone Observatory, 2015). Catchment-specific aerial imagery (Draix-Bléone Observatory, 2015) is shown alongside transparent aerial imagery of the wider area (2018 © IGN).

2.2 Drilled gas accumulation chambers

To measure in situ the production of CO₂ and consumption of O₂ by oxidative reactions in the shallow critical zone of
 135 sedimentary rocks undergoing weathering, we use drilled chambers. The chambers were visited 6 times over the study to capture seasonal changes in weather conditions, on 27/09/2018, 11/01 - 14/01/2019, 11/04 - 15/04/2019, 27/05 - 29/05/2019, 05/07 - 12/07/2019 and 27/09 - 02/10/2019. Their design has been previously detailed (Soulet et al., 2018). In summary, a horizontal chamber is drilled directly into the exposed rock which has been cleared of detrital cover. The shape of the drilled chambers ensures a large surface to volume ratio to benefit measurement of gas concentrations and potential trapping of
 140 CO₂. To install the chambers to a depth of ~ 38 cm (Fig. 2E), a mechanical drill was used with a diameter of 2.9 cm. Rock

powder left inside the chambers was blown away with a compressed-air gun. A small PVC tube was inserted in the entrance of each chamber that was closed with a rubber stopper holding two glass tubes fitted with Tygon® tubing. The latter allow either connection to a gas-sampling system or sealing with WeLock® clips. To further isolate the chamber from the atmosphere, the intersection of the PVC tube and regolith was sealed with a silicone sealant (Unibond® Outdoor), which we previously tested to be free of potential contaminants for gas sampling (Roylands et al., 2022).

At both the Brusquet and Moulin study sites, we installed one array of 4 chambers placed in a square (2×2) (Fig. 2) (Table 1). In each array, 2 chambers were placed in the same rock bed with a roughly horizontal orientation at the Brusquet site and roughly vertical at the Moulin site. The minimum distance between chambers was 70 cm. The aspect, hydrological and geomorphic setting of the location of both arrays is similar: they were placed at the upper margin of the watersheds in steep walls of gullies on a Southwest- (Brusquet) and South-facing aspect (Moulin). The chambers were drilled into bare rock faces devoid of roots and with minimal soil or vegetation cover in the vicinity to exclude a contribution by them to the CO₂ measurements (Fig. 2).

Table 1: Characteristics of gas accumulation chambers drilled into weathering sedimentary rocks in the Brusquet catchment and in the Moulin catchment. For calculation of volume and inner surface area of the chambers, length and insertion depth of the PVC tube and rubber stopper are used.

Chamber identifier		Site	Same bed as chamber	Installation date	Depth (cm)	Volume (cm ³)	Inner surface area (cm ²)
<i>short</i>	<i>long</i>						
1	M-C-1	Moulin	3	24/09/2018	41.0	278	367
2	M-A-2	Moulin	4	24/09/2018	39.5	263	346
3	M-D-3	Moulin	1	24/09/2018	38.0	255	335
4	M-B-4	Moulin	2	24/09/2018	39.0	262	345
5	B-F-5	Brusquet	6	25/09/2018	38.0	255	335
6	B-G-6	Brusquet	5	25/09/2018	37.0	255	335
7	B-H-7	Brusquet	8	25/09/2018	35.0	229	299
8	B-I-8	Brusquet	7	25/09/2018	35.0	235	308

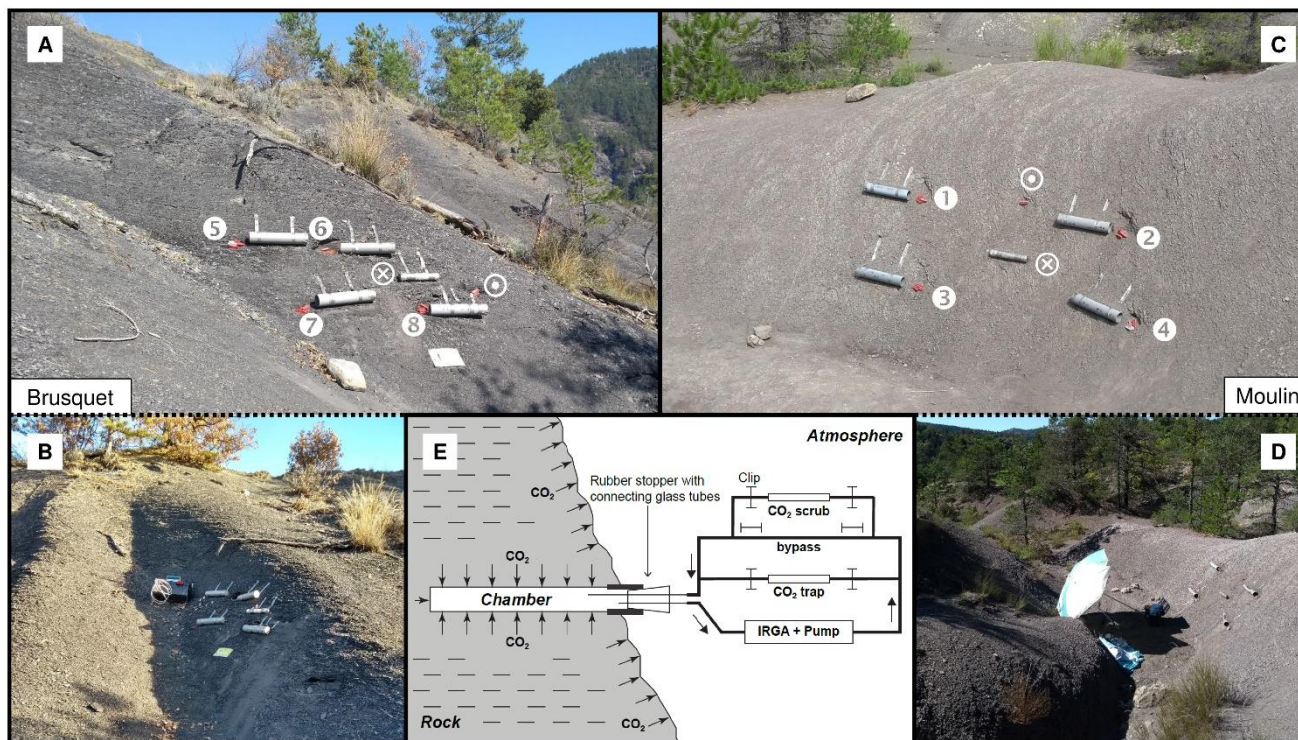


Figure 2: The study sites in the Brusquet catchment (Panels A and B) and in the Moulin catchment (Panels C and D). Identifiers of the CO₂ accumulation chambers (Table 1) are given next to their entrance. Furthermore, the location of temperature and relative humidity loggers in a further chamber with similar properties (circled dot) and on the rock surface (circled X) are shown. For scale, the grey cases (not used in the present study) next to the chambers are of ~ 40 cm length. Panel E shows the design of the chambers and the sampling system adapted from Soulet et al. (2018).

2.3 Rock temperature and humidity

At both sites, a chamber with the same design was installed to hold a temperature and relative humidity logger (Lascar® EL-USB-2) (Fig. 2) from 27/09/2018 onwards. A second logger was placed on the rock surface (monitoring the air directly above it) with the main body fitted inside a small PVC tube for physical protection and an aluminum foil wrapping around the tube to avoid alteration of the temperature measurement due to the dark color of the housing of the sensor and the PVC tube.

Over the study period, technical issues with batteries of the temperature and relative humidity loggers prevented continuous data collection. To fill the gaps in the direct chamber temperature measurements, we use air temperatures from a local weather station as a proxy (Appendix A) by modifying a framework that describes soil temperatures by, amongst other variables, air temperature (Liang et al., 2014). Using the site-specific air temperatures, this approach simulates the chamber temperature well, with a root-mean-square error (RMSE) of 1.8 °C for the Brusquet catchment and 2.2 °C for the Moulin catchment (Appendix A).

2.4 Partial pressure of rock CO₂

175 The partial pressure of CO₂ ($p\text{CO}_2$) was measured alongside air pressure to determine the concentrations of CO₂ in the rock chambers with an infra-red gas analyzer (IRGA; EGM-5 Portable Gas Analyzer, PP Systems). This is equipped with an internal pump and calibrated to $p\text{CO}_2$ in the range of 0 ppmv to 30,000 ppmv. First, the closed-loop sampling system is purged of CO₂ using an inline CO₂ scrub (soda lime) (Hardie et al., 2005). This is then connected to a chamber to measure the ambient $p\text{CO}_2$. After a short equilibration, the $p\text{CO}_2$ in the chamber ($p\text{CO}_{2\text{ Chamber}}$) is calculated from the CO₂ concentration in the combined air volume of the chamber and the sampling system by accounting for the dilution introduced from the CO₂-free air that was originally contained within the sampling system (Soulet et al., 2018; Roylands et al., 2022). To ensure that the determined $p\text{CO}_{2\text{ Chamber}}$ is representative of the ambient $p\text{CO}_2$ in the rock pores around the chamber ($p\text{CO}_{2\text{ Rock}}$), measurements are only considered if the chambers were left closed overnight so that the production of CO₂ from oxidative weathering could reach a steady-state with respect to diffusion between rock pores, chamber and atmosphere.

185 2.5 CO₂ flux measurements

Real-time measurements of CO₂ release in drilled chambers have been previously described in detail (Soulet et al., 2018) and used to quantify CO₂ flux (Soulet et al., 2021; Roylands et al., 2022). In summary, one CO₂ flux measurement consists of a series of repeated accumulations (typically 8 or more) that are recorded over time after determining the $p\text{CO}_{2\text{ Rock}}$. First, the $p\text{CO}_{2\text{ Chamber}}$ is lowered to a value close to the local atmosphere value using soda lime or a zeolite sieve (Sect. 2.6) (Fig. 2E). Then, CO₂ is allowed to build up, typically over ~ 6 min, before the CO₂ in the chamber is again removed to a near-atmospheric value. For each repeat, the rate of CO₂ accumulation q (mgC min⁻¹) is calculated by fitting an exponential model to the recorded $p\text{CO}_2$ change, following Pirk et al. (2016):

$$\frac{dm(t)}{dt} = q - \lambda (m(t) - m_0), \quad (2)$$

where $\frac{dm(t)}{dt}$ is the carbon mass change (mgC) in the chamber with time (min), m_0 is the initial carbon mass in the chamber (mgC), and λ (min⁻¹) is a constant covering the sum of all processes that are proportional to the carbon mass difference ($m(t) - m_0$) and that relate to the diffusion of CO₂ between rock pores, chamber and atmosphere (Soulet et al., 2018). For this, the carbon mass (m , mgC) in the chamber is obtained from:

$$m(t) = p\text{CO}_{2\text{ Chamber}}(t) \times V \times \frac{P}{R \times T} \times M_C \times 10^{-9}, \quad (3)$$

where the measured $p\text{CO}_{2\text{ Chamber}}$ is in ppmv (cm³ m⁻³), V is the combined volume (cm³) of the chamber and the sampling system, P is the pressure (Pa), R is the universal gas constant (m³ Pa K⁻¹ mol⁻¹), T is the chamber temperature (K), and M_C is the molar mass of carbon (g mol⁻¹).

The CO₂ accumulation rate q can be normalized to the internal surface area of the chamber S_{Chamber} (i.e., area of exchange with the surrounding rock, m²) to account for differences in the depth of the chambers, which are related to differences in volume and surface area, giving a repeat-specific flux Q (mgC min⁻¹ m⁻²):

$$205 \quad Q = \frac{q}{S_{\text{Chamber}}}. \quad (4)$$

Alternatively, the CO₂ accumulation can be reported as a molar-based flux J_{CO_2} (mmol CO₂ min⁻¹ m⁻²):

$$J_{\text{CO}_2} = \frac{j_{\text{CO}_2}}{S_{\text{Chamber}}} = \frac{q}{M_c \times S_{\text{Chamber}}}, \quad (5)$$

where j_{CO_2} (mmol CO₂ min⁻¹) is the molar-based analogue to q .

210 Previous work has noted that the CO₂ accumulation rate during the first measurements is typically higher than subsequent repeats (Soulet et al., 2018). To calculate a CO₂ flux from these repeated accumulations (consisting of n repeats), previous work excluded the first 3 repeats (q_1 to q_3), and took the average of a minimum of 3 further repeats (q_4 to $q_{n \geq 6}$) (Roylands et al., 2022; Soulet et al., 2018, 2021). We examine this further using new data collected here, which also provides constraint on the nature of the gas exchange around the chambers.

2.6 CO₂ sampling

215 During a CO₂ flux measurement, the CO₂ in the chamber can be sampled by circulating it through a zeolite molecular sieve cartridge (MSC) mounted in parallel to the monitoring line (Hardie et al., 2005; Soulet et al., 2018). The volume of carbon loaded onto a sieve is estimated by adding up the $p\text{CO}_2$ maxima for each trapping episode minus the final $p\text{CO}_2$ after trapping (near-atmospheric value), while accounting for the combined volume of the chamber and the sampling system.

The zeolite sieves were heated in the laboratory to 425 °C and purged with high-purity nitrogen gas to release the CO₂ 220 trapped onto them prior to cryogenic purification under vacuum (Garnett and Murray, 2013). The estimated sampled volume of CO₂ from the chamber-based $p\text{CO}_2$ measurements ($V_{\text{CO}_2\text{-IRGA}}$, ml) can be compared with the volume recovered from the MSC in the laboratory ($V_{\text{CO}_2\text{-MSC}}$, ml) giving a sampling ratio (SR , unitless) (Roylands et al., 2022):

$$SR = \frac{V_{\text{CO}_2\text{-MSC}}}{V_{\text{CO}_2\text{-IRGA}}}. \quad (6)$$

For this, all volumes of CO₂ are normalized to 0 °C and 1,013 mbar. The SR thus allows us to independently check 225 calculations of carbon mass using the $p\text{CO}_2$ data combined with the gas line and chamber volume measurements (Eq. 2 and 3).

2.7 Measuring $p\text{O}_2$ and O₂ fluxes

While measuring $p\text{CO}_2$, the EGM-5 Portable Gas Analyzer, incorporating the IRGA, also records the partial pressure of oxygen in the chamber ($p\text{O}_2$ Chamber, % v/v) with an electrochemical O₂ sensor. The $p\text{O}_2$ Chamber cannot be used in the same 230 way as the $p\text{CO}_2$ to quantify flux for two reasons: i) the precision of the O₂ sensor of ≥ 0.1 % (v/v) is insufficient to observe real-time changes in $p\text{O}_2$ Chamber; and ii) O₂ should be consumed during oxidative weathering and so we would require a method that replenishes oxygen, which was not done while measuring CO₂ accumulation.

An alternative method to calculate an O₂ flux is based on Fick's law (Eq. 1), using the diffusive gradient of the partial pressure of O₂ in the rock ($p\text{O}_2$ Rock) towards the atmospheric O₂ concentration ($p\text{O}_2$ Atm.). To obtain $p\text{O}_2$ Rock, the 235 $p\text{O}_2$ Chamber measured after connecting to the chamber is corrected for the oxygen concentration in the sampling system. The

pO_2 recorded before and during a measurement is corrected for instrument drift. The drift correction is based on measuring the $pO_{2 \text{ Atm.}}$ directly before or after a chamber-based measurement and assuming an average atmospheric oxygen concentration of 20.95 % (v/v).

To quantify the exchange of O_2 between the chamber, connected rock pores and the atmosphere (j_{O_2} , mmol $O_2 \text{ min}^{-1}$), we describe the process via a diffusive transfer controlled by the diffusivity of O_2 (D_{O_2} , $\text{cm}^2 \text{ min}^{-1}$) across a spatial parameter ω (describing in combination the movement across area over depth, $\text{cm}^1 \text{ cm}^{-2}$):

$$j_{O_2} = \frac{D(O_2)}{\omega} \times (pO_{2 \text{ Rock}} - pO_{2 \text{ Atm.}}) \times \frac{P}{R \times T} \times 10^{-3} . \quad (7)$$

If we assume that ω is the same for O_2 and CO_2 , linking the space of O_2 consumption and CO_2 release, D_{O_2} can be related to the diffusivity of CO_2 (D_{CO_2} , $\text{cm}^2 \text{ min}^{-1}$) based on their ideal relation in air, which is independent of temperature (Angert et al., 2015):

$$\frac{D(CO_2)}{D(O_2)} = 0.76 = \frac{D(CO_2)}{\omega} \div \frac{D(O_2)}{\omega} . \quad (8)$$

Differences in the effective diffusivities of gas species depend on the structure of the air-filled pore space, which is expected to have identical impacts on the gaseous movement of O_2 and CO_2 (Angert et al., 2015; Millington, 1959; Penman, 1940). Thus, if the term $\frac{D(CO_2)}{\omega}$ ($\text{cm}^3 \text{ min}^{-1}$) can be quantified by other means (for instance, through analysis of the $pCO_{2 \text{ Rock}}$ and CO_2 flux data), we can quantify j_{O_2} . These themes will be discussed later (Sect. 4.1 and 4.4).

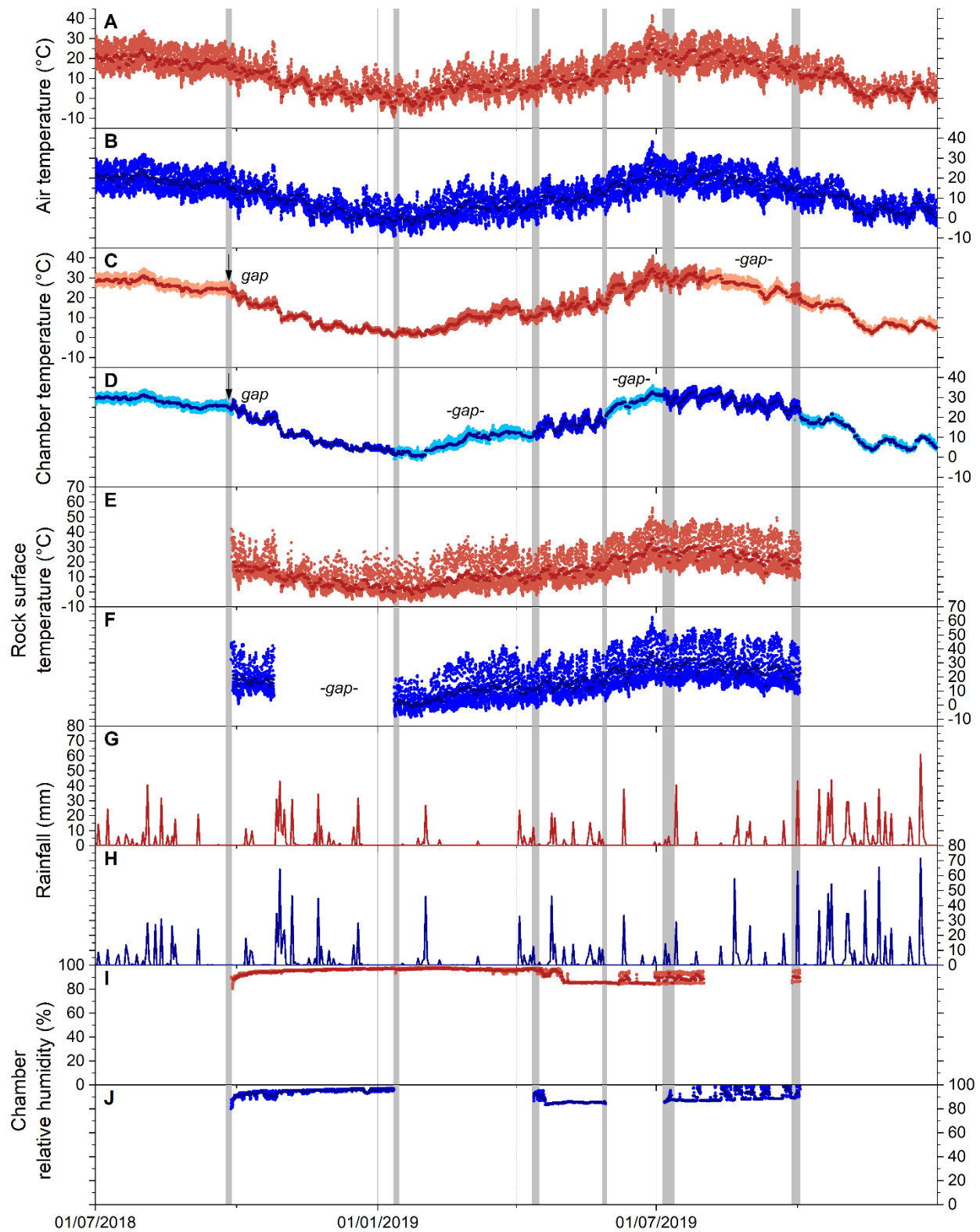
3 Results

3.1 Chamber temperature and meteorological conditions

Over the study period (27/09/2018 - 02/10/2019), similar variability in environmental conditions was recorded at the Brusquet and Moulin catchment. The temperatures of the atmosphere, chamber interiors and at the rock surface showed daily and seasonal changes (Table 2) (Fig. 3A - F). Rainfall events were comparable in occurrence and extent, but the Brusquet catchment received less cumulative rainfall (773 mm) than the Moulin catchment (1033 mm) (Fig. 3G and 3H). The relative air humidity in the chambers was high and constant with values of $\sim 93.1 \pm 4.5$ % (\pm standard deviation, SD) and $\sim 91.3 \pm 4.1$ % at the Brusquet and Moulin sites, respectively (not considering gaps in the record) (Fig. 3I and 3J).

260 **Table 2: Overview of the variability of air temperature, chamber temperature and rock surface temperature over the study period (27/09/2018 - 02/10/2019) (Fig. 3). A gap in the record of rock surface temperatures at the Moulin site (25/10/2018 - 11/01/2019) is not considered.**

Variable	Daily averages			Hourly resolution	
	Average (\pm SD)	Min.	Max.	Min.	Max.
Air temperature ($^{\circ}$ C)					
<i>Brusquet</i>	10.5 \pm 7.4	-4.9	29.5	-9.5	41.5
<i>Moulin</i>	10.5 \pm 7.3	-4.0	27.9	-9.1	38.3
Chamber temperature ($^{\circ}$ C)					
<i>Brusquet</i>	15.7 \pm 9.4	0.7	34.6	-1.1	41.0
<i>Moulin</i>	16.6 \pm 9.7	0.2	33.0	-1.5	36.1
Rock surface temperature ($^{\circ}$ C)					
<i>Brusquet</i>	14.4 \pm 8.7	-1.6	35.3	-7.0	56.0
<i>Moulin</i>	17.9 \pm 9.0	-1.4	37.3	-8.5	62.5



265 **Figure 3: Environmental variables for weathering chambers in 2018 and 2019, with grey shaded areas showing fieldwork visits, in the Brusquet catchment (Panels A, C, E, G and I; red) and in the Moulin catchment (Panels B, D, F, H and J; blue). Daily averages are shown by darker colors in all panels. Panels A and B: hourly air temperatures from meteorological stations (Draix-Bléone Observatory, 2015). Panels C and D: hourly chamber temperatures. Estimated chamber temperatures are indicated by lighter colors (Sect. 2.3) and are shown for gaps in the logger record (denoted). Panels E and F: hourly rock surface temperatures. Panels G and H: daily rainfall. Panels I and J: relative humidity in the chambers with gaps in the record similar to the chamber**
 270 **temperatures.**

3.2 $p\text{CO}_2$ measurements and CO_2 collection

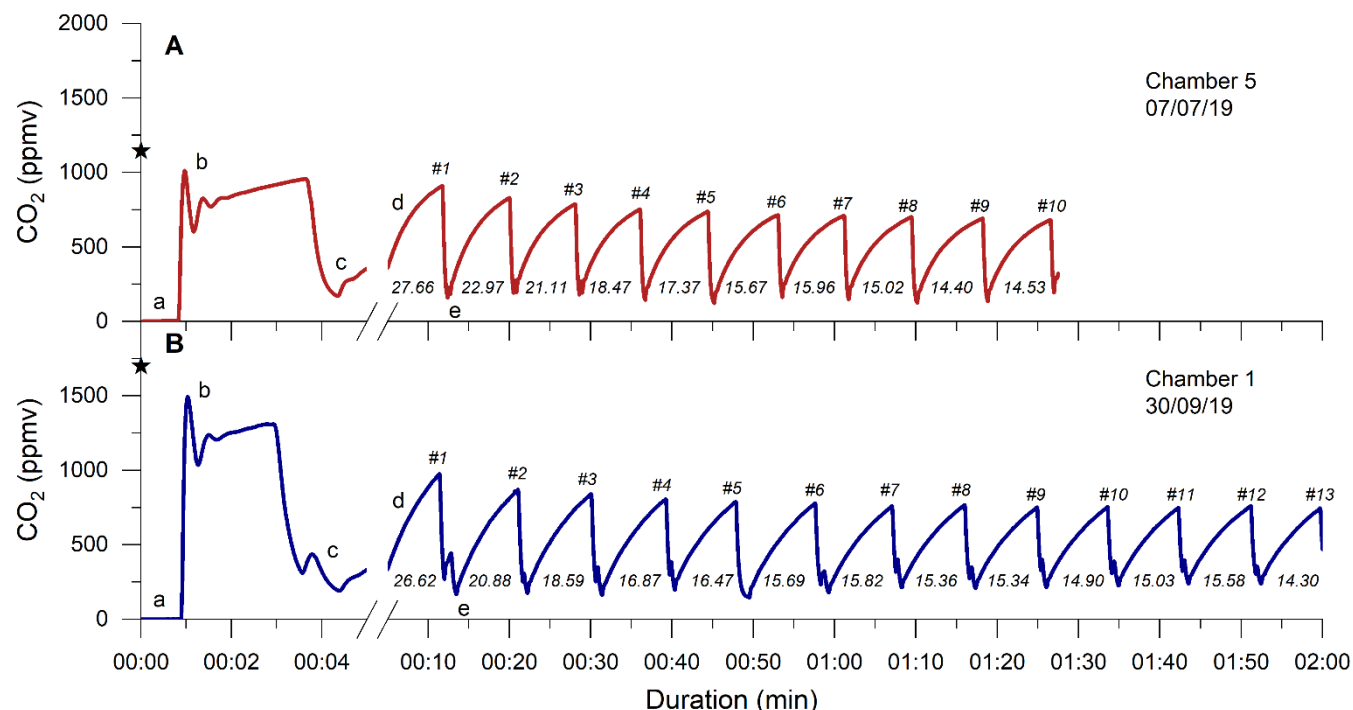
The $p\text{CO}_2$ Rock values varied between the chambers and over time. In the Brusquet catchment, the observed $p\text{CO}_2$ Rock values were on average $1,490 \pm 743$ ppmv (\pm SD, if not reported otherwise, $n = 28$), and $1,492 \pm 633$ ppmv ($n = 32$) in the Moulin catchment (Table 3).

275 **Table 3: Chamber-specific overview of $p\text{CO}_2$ Rock, with variations over time reported as 1 SD.**

Chamber identifiers		Site	$p\text{CO}_2$ Rock (ppmv)			
<i>short</i>	<i>long</i>		Average	n	Min.	Max.
5	B-F-5	Brusquet	861 ± 254	5	588	1,167
6	B-G-6	Brusquet	$1,985 \pm 771$	12	936	3,378
7	B-H-7	Brusquet	936 ± 340	4	588	1,399
8	B-I-8	Brusquet	$1,405 \pm 438$	7	721	2,000
<i>Brusquet totals</i>			$1,490 \pm 743$	28		
1	M-C-1	Moulin	$1,740 \pm 654$	10	551	2,499
2	M-A-2	Moulin	720 ± 110	4	543	834
3	M-D-3	Moulin	$1,881 \pm 127$	3	1,755	2,054
4	M-B-4	Moulin	$1,456 \pm 576$	15	681	2,680
<i>Moulin totals</i>			$1,492 \pm 633$	32		

Following the determination of $p\text{CO}_2$ Rock, a total of 37 CO_2 flux measurements were conducted in the Brusquet catchment, of which 32 consisted of ≥ 8 repeats. In the Moulin catchment, 41 measurements were made, with 37 having ≥ 8 repeats. Every individual CO_2 flux measurement showed an initial decline of accumulation rates that approached a constant value of peak CO_2 concentration (Fig. 4). Considering the repeats 6 - 8, averages of the CO_2 accumulation rates varied
 280 between chambers and over time at each single chamber, with occurrence of the lowest accumulation rates in winter and highest in summer. On four visits, a chamber was measured twice a day and the observed CO_2 release was higher in the afternoon than in the morning, coinciding with an increase of the chamber temperature. Overall, the observed CO_2 accumulation rates (averages of q_6 to q_8) were on average 15.2 ± 11.7 $\mu\text{gC min}^{-1}$ ($n = 32$) and 11.5 ± 8.0 $\mu\text{gC min}^{-1}$ ($n = 37$) in the Brusquet catchment and in the Moulin catchment, respectively. The associated values of the fitting parameter λ (Eq. 2)
 285 were on average of 0.179 ± 0.076 min^{-1} ($n = 32$) and 0.140 ± 0.061 min^{-1} ($n = 37$) in the Brusquet catchment and in the Moulin catchment, respectively.

At each study site, CO₂ was sampled from two chambers. Following recovery from the zeolite sieves in the laboratory, the sampling ratio (*SR*, Eq. 6) was quantified with an overall average of 1.00 ± 0.15 (Table 4).



290 **Figure 4:** Two examples of monitoring the CO₂ concentration (ppmv) in a chamber during a flux measurement. Following
 connection, the CO₂-free air of the sampling system (a) equilibrates with the partial pressure of CO₂ in the chamber (b), which is
 representative of $p\text{CO}_2$ Rock (denoted by ★). After the CO₂ in the chamber is removed to a near-atmospheric value (sometimes
 stepwise, c), the first accumulation (d) is monitored (with a change in x-axis scale), followed by further removal (e) and
 295 accumulation events (~ 6 min, numbers denoted with #). The measured accumulation rates (q , $\mu\text{gC min}^{-1}$ per chamber) are given
 for each repeat. The CO₂ flux measurement of chamber 5 on the 07/07/19 (Brusquet catchment, Panel A, red) consists of 10
 repeats, and the measurement of chamber 1 on the 30/09/19 (Moulin catchment, Panel B, blue) consists of 13 repeats.

Table 4: Overview of the chamber-specific sampling ratio (*SR*, Eq. 6), which compares the estimated volumes of CO₂ sampled in
 the Brusquet catchment and in the Moulin catchment with volumes recovered in the laboratory from zeolite sieves.

Chamber identifiers		Site	Number of samples	Sampling ratio (<i>SR</i> , unitless)		
<i>short</i>	<i>long</i>			Median	Average (± 1 SD)	
1	M-C-1	Moulin	4	0.90	0.98	± 0.25
4	M-B-4	Moulin	7	0.93	0.94	± 0.10
6	B-G-6	Brusquet	7	1.04	1.05	± 0.09
8	B-I-8	Brusquet	2	1.12	1.12	± 0.04
<i>Totals</i>			20	1.03	1.00	± 0.15

3.3 $p\text{O}_2$ measurements

300 The total number of usable $p\text{O}_2$ Chamber measurements was limited to 15. The difference in $p\text{O}_2$ between the chambers and the atmosphere ($p\text{O}_2$ Chamber - $p\text{O}_2$ Atm.) varied over time, ranging from zero within uncertainty (0.18 ± 0.36 %, v/v, ± 95 % confidence interval, CI) to -1.50 ± 0.30 % (v/v), with the lowest $p\text{O}_2$ Chamber values in summer and higher values (lower gradient) in winter at both sites (Fig. 12A).

4 Discussion

305 Carbon dioxide release during oxidative weathering of sedimentary rocks exposed in steep mountain areas has been shown to vary with changes in temperature, precipitation and local topography (Soulet et al., 2021; Roylands et al., 2022). Furthermore, previous studies on weathering profiles (Bolton et al., 2006; Petsch, 2014) and on the chemical composition of rivers (Calmels et al., 2007; Bufe et al., 2021; Hilton et al., 2021) indicated that geomorphological and hydrological factors are important controls on the release of CO_2 and the consumption of O_2 during oxidative weathering. The fluxes should also
310 depend on the pore space characteristics of the weathering zone, such as porosity and tortuosity (Bolton et al., 2006; Brantley et al., 2013; Gu et al., 2020a, b; Soulet et al., 2021). However, we lack direct observations of how the chemical and physical properties of the weathering zone affect the in situ fluxes of CO_2 and O_2 . In addition, only with information on the contributing rock volume to a measured rock-derived flux can we upscale and quantify CO_2 and O_2 fluxes from the measurement site to the landscape scale.

315 In the following discussion, we first propose a new approach of interpreting in situ CO_2 flux measurements (Sect. 4.1.1) that allows us to assess the diffusion of CO_2 and O_2 in the shallow critical zone (Sect. 4.1.2). This can be used to quantify the rock volume contributing to the measured fluxes (Data-flow diagram in Appendix B) (Sect. 4.2). We then examine the implications of these new insights for quantifying the rock-derived CO_2 release (Sect. 4.3), and then determine the coinciding O_2 consumption (Appendix B) to investigate an overall redox budget of oxidative weathering in an erosive
320 environment (Sect. 4.4).

4.1 Probing the gas exchange of the shallow critical zone

4.1.1 Explaining the patterns of CO_2 accumulation during a single flux measurement

To explain the initial decline of CO_2 accumulation rates during a flux measurement that stabilizes over time (Fig. 4), we consider the known volume of a drilled chamber and distinguish it from the unknown rock pore space around it. After
325 arriving at a chamber to start a CO_2 flux measurement, the initial scrubbing (before the first repeat q_1) removes CO_2 from the chamber (i.e., $p\text{CO}_2$ Chamber) to a near-atmospheric level, but we assume that it does not remove the CO_2 from the connected pore space to a similar $p\text{CO}_2$ value. Repeated scrubbing and removal of CO_2 after CO_2 accumulations (Fig. 4) then acts to lower the CO_2 concentration in the rock pore space connected to the chamber ($p\text{CO}_2$ Rock). In this process, rock pores that are

330 better connected to the chamber (i.e., that have a shorter effective diffusion pathway) provide the initially stored CO₂ earlier compared to rock pores that are less connected. In contrast, rock pores that are connected better to the atmosphere than to the chamber are assumed to contribute only to the atmosphere. Once the pool of “excess” CO₂ in the pore space that is effectively connected to the chamber has been exhausted, subsequent CO₂ accumulation rates reach a plateau and are assumed to represent the real-time production and diffusion of CO₂ in the rock surrounding the chamber. This explanation requires that the air volume processed by the sampling system equals the chamber volume, whereas the gas exchange
335 between chamber and connected rock pores happens solely via diffusion. This assumption is supported by the measured CO₂ sampling ratio, *SR* (Eq. 6), with an average $SR = 1.00 \pm 0.15$ (Table 4), showing we effectively trap the chamber contents. This is similar to the recovery efficiency of ~ 95 % of CO₂ standards in the laboratory (Garnett et al., 2019).

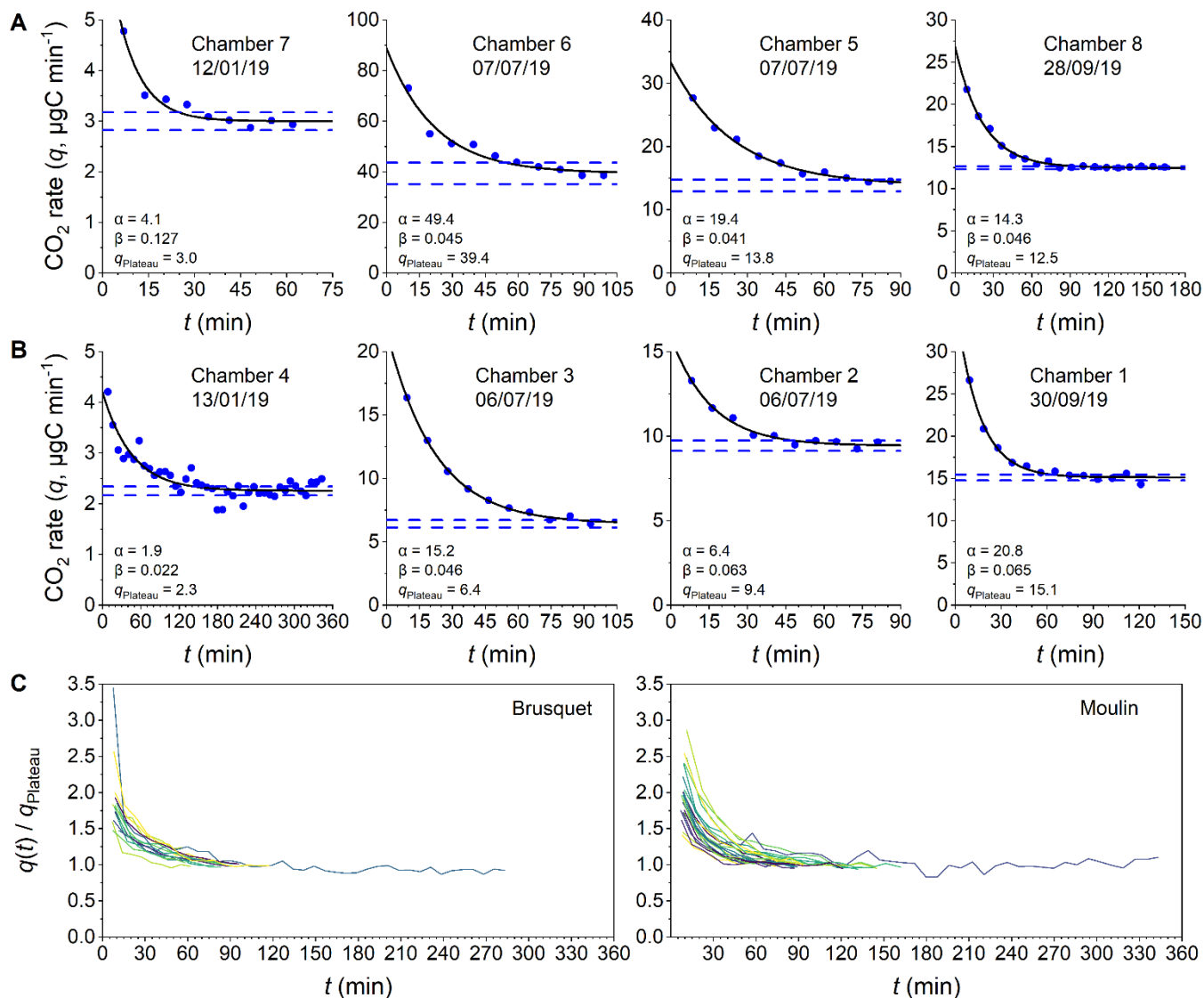
To interpret the period where we consider an excess of CO₂ is diffusing into the chamber from a connected pore space, we introduce an exponential fitting model that describes the decrease of CO₂ accumulation rates (*q*) over time (Fig. 5):

$$340 \quad q(t) = \alpha \times \exp(-\beta \times t) + q_{\text{plateau}}, \quad (9)$$

where q_{plateau} is a constant value of the plateaued CO₂ accumulation rate, the sum of α and q_{plateau} is the initial rate of accumulation ($\approx q_1$, mgC min⁻¹) at the start of the flux measurement ($t = 0$), β is the measurement-specific removal constant (min⁻¹), and the term $\alpha \times \exp(-\beta \times t)$ describes the purging of the initially stored *p*CO₂ from the rock pore space connected to the chamber over time.

345 To ensure reliable results from fitting the exponential model, measurements are only considered if the last 3 of at least 8 repeats (q_{n-2} to q_n for $n \geq 8$) are “stabilized”, which we define as having a relative standard deviation of less than 5 %. To interpret the remaining CO₂ flux measurements, chamber-specific averages of the removal constant β from stabilized measurements are used to extrapolate q_{plateau} for measurements that did not stabilize.

The outputs of this analysis provide a CO₂ flux that represents the real-time production of CO₂ (q_{plateau}), while
350 quantifying the scrubbing of CO₂ stored initially in the connected volume of pore space around each chamber. This allows us to assess the diffusive movement of CO₂ in the shallow weathering zone (Sect. 4.1.2) and to estimate the contributing rock volume (Sect. 4.2) (Appendix B).



355 **Figure 5: Examples of CO₂ flux measurements consisting of several repeated accumulation rate measurements. Measured accumulation rates (q , $\mu\text{gC min}^{-1}$ per chamber, y-axis) are shown alongside exponential fits (Eq. 9) describing their evolution over time (x-axis) and alongside the 95 % confidence intervals of the modeled level at which the rates plateau (q_{plateau}) for chambers in the Brusquet catchment (Panel A) and in the Moulin catchment (Panel B). Dates and fitting parameters α ($\mu\text{gC min}^{-1}$) and β (min^{-1}) of the single flux measurements, indicated by varying colors, $q(t)$ is normalized to q_{plateau} for both study sites in separate plots (Panel C).**

360 4.1.2 Assessing the diffusivity of the shallow weathering zone

After a CO₂ flux measurement, the chamber is re-sealed. The chamber interior and surrounding pore space will evolve to a steady-state of diffusive movement of CO₂ along a concentration gradient between the surface of the rock outcrop and the atmosphere so that $p\text{CO}_2_{\text{Chamber}} = p\text{CO}_2_{\text{Rock}}$. Thus, this steady-state of a closed chamber differs from the manipulated environment of a CO₂ flux measurement (Fig. 4). The comparison of the two states can shed light on gas movement and the

365 physical properties of the rocks undergoing weathering. Here, we explore how the observed changes in $p\text{CO}_2\text{ Rock}$ and CO_2 fluxes can be explained by a framework of diffusive processes in the shallow critical zone, and assess the degree to which these are modulated by weather conditions.

According to Fick's law (Eq. 1), diffusion of gases in a porous medium is controlled by: i) the production and accumulation of CO_2 ; ii) the volume of space (rock pores and/or chamber) and length scale over which molecules travel
370 towards the low- $p\text{CO}_2$ reservoir; and iii) the diffusivity of CO_2 along their path. We find a co-variation of $p\text{CO}_2\text{ Rock}$ and the CO_2 fluxes that is similar for both sites, a relationship that can be explained by a linear regression model (Appendix C), with high $p\text{CO}_2\text{ Rock}$ values coinciding with high CO_2 accumulation rates (Fig. 6A). This indicates that the contributing volume of rock pores and the diffusivity (the remaining variables from Fick's law) may be stable at both sites over the study period.

However, the ambient hydroclimate appears to modify the response of these variables. We consider measurements
375 as being made during "wet" or "dry" periods, whereby "wet" measurements are those where the cumulative precipitation over the last 3 days was ≥ 5 mm. At a given $p\text{CO}_2\text{ Rock}$ value (describing the storage of CO_2 in the shallow critical zone), "dry" conditions are associated with lower CO_2 production compared to "wet" conditions (Fig. 6A). With respect to the CO_2 production, previous research has shown that rock-derived CO_2 fluxes from drilled chambers are lower following rain events, but recover subsequently over a few dry days (Soulet et al., 2021; Roylands et al., 2022). This latter observation has
380 been linked to the degree of water saturation controlling the gas motion in the pore space and thus the supply of O_2 for the oxidative weathering reactions, as well as to dissolution of weathering derived carbon and subsequent export of dissolved inorganic carbon (DIC) (Soulet et al., 2021; Roylands et al., 2022). It is important to note that a decrease of the production of CO_2 , associated with a lower O_2 supply and/or with a greater uptake of carbon into the DIC, leads also to a proportional decrease in $p\text{CO}_2\text{ Rock}$ values (Roylands et al., 2022; Soulet et al., 2021). To understand the changes in the relation of
385 $p\text{CO}_2\text{ Rock}$ and CO_2 flux during "wet" and "dry" conditions, a change in the diffusivity of the contributing rock volume needs to be considered.

According to Fick's law, a lower diffusivity at a constant contributing volume of rock results in higher $p\text{CO}_2\text{ Rock}$ values. Thus, "wet" conditions may be associated with a decrease in the diffusivity of gases in the weathering rocks. This fits a simple model describing the effective diffusivity D_{Rock} ($\text{m}^2 \text{s}^{-1}$) of a given gas in porous media (such as rocks and soils) at a
390 given temperature by:

$$D_{\text{Rock}} = D_{\text{Air}} \times \varphi_{\text{Air-filled}} \times \tau, \quad (10)$$

where D_{Air} is the diffusion coefficient ($\text{m}^2 \text{s}^{-1}$) of the particular gas in air, τ is a dimensionless tortuosity factor, and $\varphi_{\text{Air-filled}}$ is the air-filled porosity (v/v %) (Penman, 1940; Davidson and Trumbore, 1995). If $\varphi_{\text{Air-filled}}$ decreases due to meteoric water filling the pore space, precipitation events lower the effective diffusivity of CO_2 within the critical zone (Sánchez-Cañete et al., 2018). An increase of moisture in porous media also leads to more tortuous pathways (Millington, 1959; Davidson and Trumbore, 1995), which could further lower D_{Rock} under wet conditions. Analogously, rock moisture would also affect the diffusion of atmospheric O_2 into the rock pore space, so that this framework can explain the observed decrease of CO_2 production following rain events (Roylands et al., 2022; Soulet et al., 2021).

To describe the diffusion of CO₂ during the steady-state of a closed chamber, we use Fick's law (Eq. 1) and the measured CO₂ flux (q_{plateau}) and the concentration gradient of CO₂ ($p\text{CO}_2_{\text{Rock}} - p\text{CO}_2_{\text{Atm.}}$) to define a measure ($\frac{D(\text{CO}_2)}{\omega}$, cm³ min⁻¹) that describes the effective diffusivity D_{CO_2} (cm² min⁻¹) of the CO₂ flux towards the atmosphere over the unknown effective depth and area ω (cm¹ cm²):

$$\frac{D(\text{CO}_2)}{\omega} = \frac{q_{\text{plateau}}}{p\text{CO}_2_{\text{Rock}} - p\text{CO}_2_{\text{Atm.}}} \times \frac{R \times T}{P} \times \frac{10^9}{M_c}. \quad (11)$$

The calculated values (based on repeats 6 - 8) are on average 27.5 ± 12.4 cm³ min⁻¹ (n = 25) and 21.8 ± 13.2 cm³ min⁻¹ (n = 30) for the Brusquet catchment and the Moulin catchment, respectively.

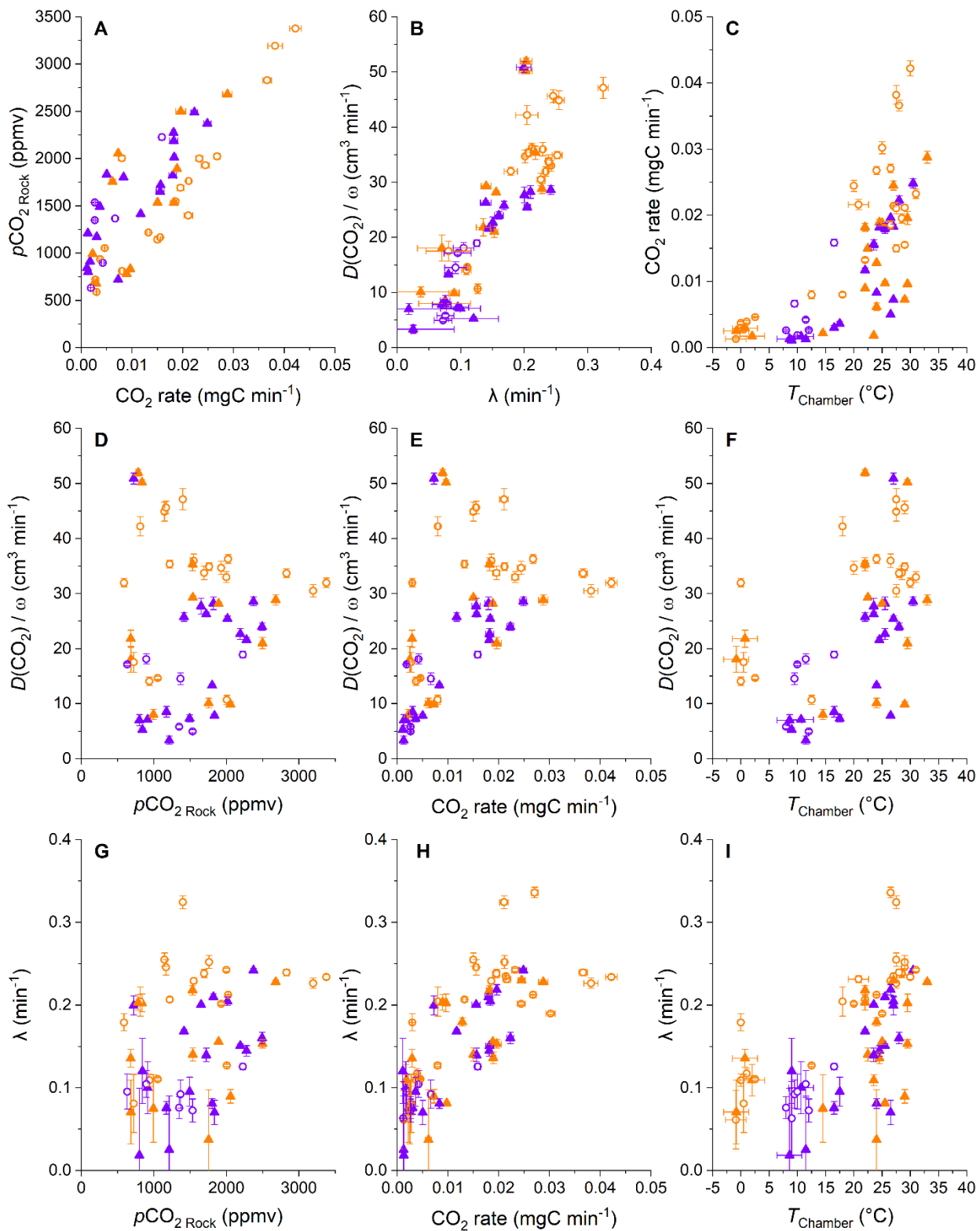
An alternative way to assess diffusivity is to use the constant λ (Eq. 2) describing the curvature of the repeated accumulations during a CO₂ flux measurement (Fig. 4) (Pirk et al., 2016). Differences between λ and $\frac{D(\text{CO}_2)}{\omega}$ may be expected because λ is representative of short intervals (~ 6 min observations), while $\frac{D(\text{CO}_2)}{\omega}$ represents a period of a few hours. We find a significant linear correlation of λ and $\frac{D(\text{CO}_2)}{\omega}$ for all samples irrespective of the study site (Fig. 6B) (Appendix D). The similarities of both metrics affirm that the accumulation rates determined during flux measurements are representative for the longer-term CO₂ release towards the atmosphere.

The concordance of changes in λ and in $\frac{D(\text{CO}_2)}{\omega}$ suggests that the rock pore space is relatively homogenous in porosity and tortuosity, since the diffusive pathways of the steady-state during a stabilized flux measurement differ from that of a closed chamber (Appendix E). Minor heterogeneities may explain some scatter in the correlation of λ and $\frac{D(\text{CO}_2)}{\omega}$, as well as short-term changes in the effective rock space contributing CO₂ to a chamber induced by percolation of meteoric waters.

In more detail, we find some variability in the measures of diffusivity linked to the hydroclimatic conditions. "Wet" conditions coincide generally with somewhat lower $\frac{D(\text{CO}_2)}{\omega}$ values for a given λ (Fig. 6B) (Appendix D). Because the atmosphere is acting as the low- $p\text{CO}_2$ reservoir during the steady-state of a closed chamber, $\frac{D(\text{CO}_2)}{\omega}$ is likely to be more influenced by surficial processes than λ , which is affected by CO₂ migration pathways towards the chamber (Appendix E). For example, lower $\frac{D(\text{CO}_2)}{\omega}$ values for a given λ may be the result of filling of surficial cracks with water, or micro-landslides, swelling of the surface rock material and lateral expansion following rainfall events (Bechet et al., 2015), which may hinder the migration of gas. During drier conditions, cracks may significantly increase gas exchange between the rocks and the atmosphere (Weisbrod et al., 2009; Maier and Schack-Kirchner, 2014). In the study area, desiccation cracks typically appear at steep slopes during summer, when erosion by runoff is less prevailing than in spring and autumn, whereas a thick layer of loose detrital cover can be accumulated during winter due to frost weathering (Ariagno et al., 2022, 2023), when movement of surface materials is limited to solifluction (Bechet et al., 2016). Thus, the diffusivity of the rock surface presumably changes over time, with greater values during dry summer conditions (Fig. 6F and 6I).

The λ and $\frac{D(\text{CO}_2)}{\omega}$ values can also be explored as a function of temperature inside the chambers (Fig. 6F and 6I). In air, the diffusion coefficient of CO_2 is strongly controlled by temperature with an increase by a factor of ~ 1.25 at $35\text{ }^\circ\text{C}$ compared to $0\text{ }^\circ\text{C}$ (Massman, 1998). However, we find a much larger change of λ and $\frac{D(\text{CO}_2)}{\omega}$, with an average increase by a factor of ~ 3.5 between $0\text{ }^\circ\text{C}$ and $35\text{ }^\circ\text{C}$ (Fig. 6F and 6I). This relation between temperature and diffusivity could be explained by a coinciding decrease of rock moisture. In the marls of the Laval catchment, neighboring the studied Moulin catchment, lower near-surface water contents were observed during dry summer periods, with values as low as $\sim 10\%$ contrasting to values of up to $\sim 25\%$ in winter (Mallet et al., 2020). However, the relation of rock moisture and temperature is not straightforward (Soulet et al., 2021), with precipitation being an important control on surface rock moisture. In addition, we observe high and constant relative air humidity in the chambers over the year (Fig. 3). Together, a complex hydrological control on D_{Rock} , which includes surface processes, may explain some part of the high apparent temperature sensitivity of λ and $\frac{D(\text{CO}_2)}{\omega}$ by modifying τ and $\phi_{\text{Air-filled}}$ (Eq. 10), alongside changes of D_{Air} forced solely by temperature.

In summary, disentangling diffusive processes in the shallow weathering zone is complicated by drivers that can be interrelated and co-vary (Fig. 6). This is also commonly observed in soils (Hashimoto and Komatsu, 2006; Maier and Schack-Kirchner, 2014; Davidson and Trumbore, 1995; Tokunaga et al., 2016). Generally, hydrology and temperature are important controls on $p\text{CO}_2_{\text{Rock}}$, CO_2 flux, diffusivity and potentially rock pore space, all of which contribute to the release of CO_2 to the atmosphere. Interestingly, similar responses to changes in environmental controls are observed at both study sites, and they appear to have similar diffusivity measures. However, the CO_2 fluxes differ significantly between sites, with greater CO_2 efflux at a given rock temperature from the chambers in the Brusquet catchment compared to the Moulin catchment (Fig. 6C), which may be explained by a difference in the source of CO_2 or by differences in the contributing rock volume (Sect. 4.2).



450 **Figure 6: Comparisons of the diffusivity measures λ and $\frac{D(\text{CO}_2)}{\omega}$, CO₂ accumulation rates, $p\text{CO}_2\text{Rock}$ values and chamber temperatures. Color coding differentiates “dry” (orange) from “wet” samples (violet) using an approximate threshold of a cumulative precipitation of 5 mm over the last 3 days. The origin of samples is indicated with open circles for the Brusquet catchment and filled triangles for the Moulin catchment. For consistency, all parameters determined during CO₂ flux measurements are calculated on the basis of the repeats 6 - 8 (error bars: 1 SD). Estimated temperatures are indicated by accompanying error bars (RMSE).**

455 4.2 Assessing the contributing rock pore volume

4.2.1 Quantification of the contributing rock pore volume

Chamber-based measurements of CO₂ flux provide insight on the variability of fluxes over time and the environmental controls that force them (e.g., Bond-Lamberty and Thomson, 2010; Oertel et al., 2016; Pirk et al., 2016; Roylands et al., 2022; Soulet et al., 2021). However, the volume of material that contributes to the measured CO₂ fluxes is rarely quantified.

460 If this could be determined, the production of CO₂ can be considered in terms of the mass of reactants, allowing comparisons between different field sites and laboratory experiments (e.g., Angert et al., 2015; Kalks et al., 2021; Lefèvre et al., 2014; Soucémariadin et al., 2018; Tokunaga et al., 2016). In the case of the internal rock chambers used here, quantification of the contributing rock volume would allow us to upscale the fluxes over an outcrop surface area. To do this, we use the exponential fitting model (Eq. 9) that describes the transition between a closed chamber and the manipulated state during

465 flux measurements (Fig. 4 and 5) as a way to quantify the carbon mass derived from the rock pore space. By doing so, we can use the $p\text{CO}_2\text{Rock}$ to calculate the corresponding air volume in the rock volume contributing CO₂. The volume of rock pores, in turn, is used to estimate the corresponding rock volume and its geometry, and, ultimately, the rock mass to determine an absolute weathering flux.

First the mass of CO₂ purged during a flux measurement from the rock pore space around the chamber is described

470 as an excess of CO₂ (CO₂ Excess, mgC):

$$\text{CO}_2 \text{ Excess} = \int_{t(0)}^{t(\text{Plateau})} \alpha \times \exp(-\beta \times t) dt, \quad (12)$$

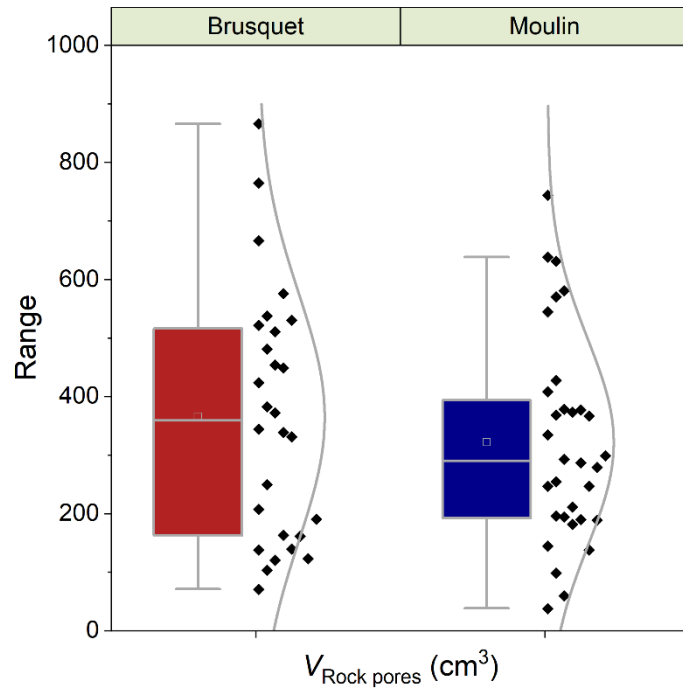
with α and β being the fitting parameters from the same fitting procedure used to calculate q_{Plateau} (Eq. 9) over time, starting at the beginning of the flux measurement ($t = 0$) and ending when the integrated term approaches zero (t_{Plateau} , when $q(t)$ equals q_{Plateau}). The air volume of the rock pores can be estimated from CO₂ Excess by using the $p\text{CO}_2\text{Rock}$ at the start of the flux

475 measurement (when $p\text{CO}_2\text{Rock}$ equals $p\text{CO}_2\text{Chamber}$). This air volume ($V_{\text{Rock pores}}$, cm³) is calculated by modifying Eq. 3:

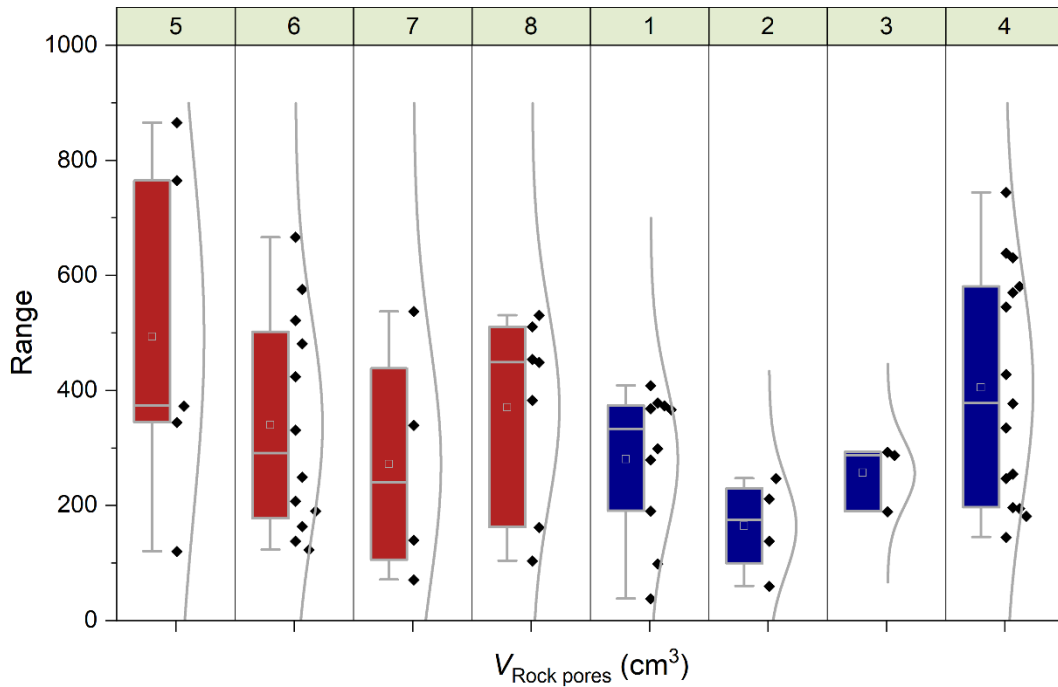
$$V_{\text{Rock pores}} = \text{CO}_2 \text{ Excess} \times \frac{R \times T}{P} \times \frac{10^9}{M_c \times p\text{CO}_2\text{Rock}}. \quad (13)$$

Overall, the calculated values of $V_{\text{Rock pores}}$ are similar for both study sites with $365 \pm 208 \text{ cm}^3$ (± 1 SD of the average of measurement-specific values) for the chambers in the Brusquet catchment, and $322 \pm 174 \text{ cm}^3$ for the chambers in the Moulin catchment (Fig. 7) (Table 5). However, significant variation is observed over time for each chamber (Fig. 8), while

480 each measurement-specific value of $V_{\text{Rock pores}}$ is associated with a high uncertainty (Table 5). These uncertainties are not normally distributed, with an average upper relative uncertainty of $125.8 \pm 140.1 \%$ (average of 95 % CI ± 1 SD) and an average lower relative uncertainty of $47.8 \pm 42.3 \%$ for all samples.



485 **Figure 7: Catchment-specific box plots and distribution curves summarizing the volume of rock pores ($V_{\text{Rock pores}}$) connected to each chamber determined during CO_2 flux measurements including 4 chambers at each site. Boxes indicate the 25 % - 75 % range alongside the 1.5 interquartile ranges with mean (open square) and median (line). Colors indicate the origin (Brusquet: red, Moulin: blue).**

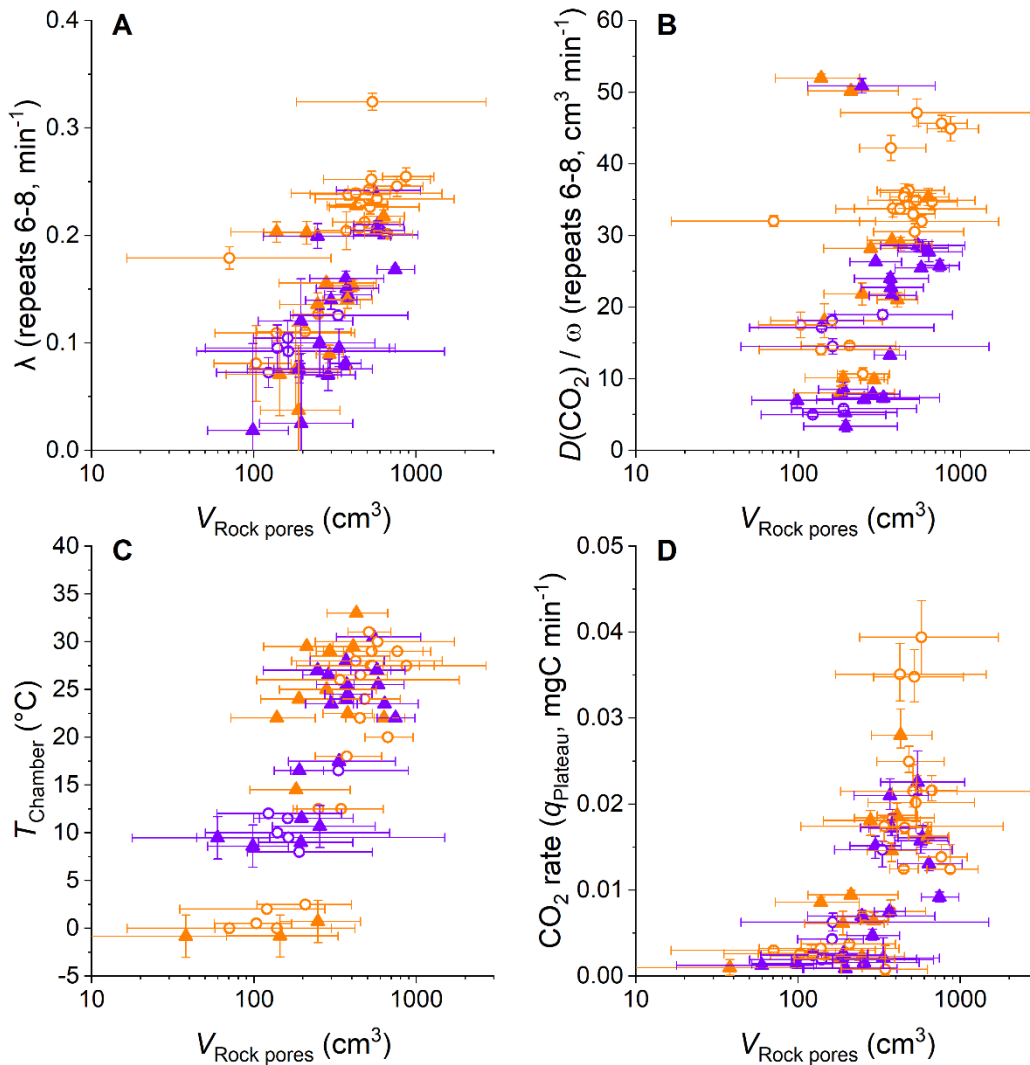


490 **Figure 8: Chamber-specific box plots and distribution curves summarizing the volume of rock pores ($V_{\text{Rock pores}}$) connected to each chamber determined during CO₂ flux measurements. Boxes indicate the 25 % - 75 % range alongside the 1.5 interquartile ranges with mean (open square) and median (line). Panels at the top show the chamber identifiers (Table 1) and colors indicate the origin (Brusquet: red, sites 5 - 8; Moulin: blue, sites 1 - 4).**

4.2.2 Environmental controls on the contributing rock pore volume

The variation of $V_{\text{Rock pores}}$ may be linked to changes in the diffusive processes and weather conditions (Fig. 9). Overall, higher values of λ coincide with greater values of $V_{\text{Rock pores}}$ (all samples: R^2 of a linear regression = 0.52, $p = <0.001$, $n = 55$) (Fig. 9A). This is also true for the relation between $V_{\text{Rock pores}}$ and $\frac{D(\text{CO}_2)}{\omega}$ (Fig. 9B), which itself is positively correlated to λ (Sect. 4.1). These relationships are similar for both sites, and for “wet” and “dry” conditions. The latter observation indicates that rock moisture impacts the diffusivity of CO₂ and $V_{\text{Rock pores}}$ in equal measure. This, in turn, is in line with Fick’s law, with the extent of the rock pore space that contributes CO₂ to a chamber depending on the potential of gas to move within the rocks undergoing weathering. In this process, the degree to which changes in the diffusivity impact the contributing rock volume is driven by the effective change in length of the diffusion paths. Here, a change of λ from 0.1 min⁻¹ to 0.2 min⁻¹ is associated with a change of $V_{\text{Rock pores}}$ by a factor of ~ 3.5 and this roughly fits the modification of the geometry of a cylinder-shaped rock pore space around a drilled chamber when doubling its effective radius.

500 Furthermore, differences in $V_{\text{Rock pores}}$ coincide with changes in temperature (all samples: R^2 of a linear regression = 0.47, $p = <0.001$, $n = 60$) (Fig. 9C). This coincidence is important to consider when assessing the control of temperature on the CO₂ production from chemical weathering (i.e., weathering kinetics), and is discussed later (Sect. 4.3). The coincidence of positive correlations of temperature and CO₂ production, and of temperature and the extent of $V_{\text{Rock pores}}$ (indirectly connected by D_{CO_2}) also suggests that changes in CO₂ flux are associated with changes in the contributing rock pore space (all samples: R^2 of a linear regression = 0.42, $p = <0.001$, $n = 60$) (Fig. 9D).



510

Figure 9: Comparisons of $V_{\text{Rock pores}}$, the diffusivity measures λ and $\frac{D(\text{CO}_2)}{\omega}$, CO_2 accumulation rates, and chamber temperatures. Color coding differentiates “dry” (orange) from “wet” samples (violet) using an approximate threshold of a cumulative precipitation of 5 mm over the last 3 days. The origin of samples is indicated with open circles for the Brusquet catchment and filled triangles for the Moulin catchment. Reported values of λ and $\frac{D(\text{CO}_2)}{\omega}$, are based on the repeats 6 - 8 of a CO_2 flux measurement (error bars: 1 SD), whereas the calculation of $V_{\text{Rock pores}}$ (displayed on a logarithmic scale) and CO_2 accumulation rates are based on the fitting model (error bars: 95 % CI). Estimated temperatures are indicated by accompanying error bars (RMSE).

515

4.2.3 Upscaling chamber-based CO_2 fluxes

The determined $V_{\text{Rock pores}}$ can be combined with the porosity of the rocks undergoing weathering to quantify the volume of rock contributing CO_2 to flux measurement (V_{Rock} , cm^3):

520

$$V_{\text{Rock}} = \frac{V_{\text{Rock pores}}}{\varphi_{\text{Air-filled}}} . \quad (14)$$

This assumes that the majority of rock pores are well connected (total porosity \approx connected porosity), with no significant water filling of the pore space. An effective air-filled porosity of 25 %, within a 95 % confidence interval of 15 % - 35 %, is assumed based on porosity measurements (Garel et al., 2012; Mallet et al., 2020) and water saturation measurements (Mallet et al., 2020) from the Draix-Bléone observatory.

On average, CO₂ fluxes from chambers in the Brusquet catchment derive from a rock volume of $1,459_{-858}^{+4,270}$ cm³ (within a 95 % confidence interval based on propagating the uncertainties of the fitting procedure and of the assigned porosity), which is similar to the release of CO₂ in the Moulin catchment from rock volumes of $1,286_{-696}^{+2,284}$ cm³. If we visualize these volumes as a cylindrical rock layer around the drilled chambers (Fig. 2E: sampling distance indicated by arrows pointing towards the chamber), its thickness would be $\sim 2.2_{-1.0}^{+2.6}$ cm. However, the geometry of this space is unknown. Instead, considering that porosities are highest at the surface of rock outcrops in the study area (Mathys and Klotz, 2008; Lofi et al., 2012; Maquaire et al., 2002; Travelletti et al., 2012; Mallet et al., 2020), where unloading and climatic controls on physical weathering act most efficiently (Bechet et al., 2016; Mathys and Klotz, 2008; Bechet et al., 2015; Cras et al., 2007; Ariagno et al., 2022), the shape of the porous and permeable rock that contributes to gas exchange is likely to be more like a cone around a chamber with a radius that declines over depth.

The knowledge of the probed layer thickness can be combined with the inner surface area of the chambers to give the spatial parameter ω (Eq. 11) and to calculate the effective diffusivity of CO₂ in the air-filled rock pores zone. Overall, we find values of D_{CO_2} ranging between ~ 0.02 cm² min⁻¹ and ~ 0.34 cm² min⁻¹ (considering the range of $\frac{D(\text{CO}_2)}{\omega}$ at both study sites; Sect. 4.1). Interestingly, these values are similar to diffusion coefficients that were determined by laboratory experiments (despite potential differences in rock texture and pore space geometry), with O₂ as the tracer gas at 22.5 °C, which correspond to D_{CO_2} values of 0.34 cm² min⁻¹ and 0.43 cm² min⁻¹ for limestones with porosities of 40 % and 46 %, and of 0.04 cm² min⁻¹ and 0.17 cm² min⁻¹ for mudstones with porosities of 33 % and 38 %, respectively (Peng et al., 2012).

The rock volume around a chamber can be “unwrapped” to assess a surface area on an outcrop that would have the same contributing rock pore volume (S_{Rock} , cm²). This can be done if the weathering depth z_{Rock} (cm) over that CO₂ is thought to be produced by oxidative weathering is considered:

$$S_{\text{Rock}} = \frac{V_{\text{Rock}}}{z_{\text{Rock}}}. \quad (15)$$

The z_{Rock} value can be estimated from the morphology of bare surfaces in the study area, based on the assumption that oxidative weathering of sedimentary rocks occurs roughly at the same depths where physical properties are altered (Gu et al., 2020a, b; Lebedeva and Brantley, 2020; Brantley et al., 2013). Based on previous research in a neighboring catchment (Maquaire et al., 2002; Mathys and Klotz, 2008; Oostwoud Wijdenes and Ergenzinger, 1998; Rovéra and Robert, 2006), physical alteration mostly occurs to depths of $\sim 10.0_{-5.0}^{+20.0}$ cm at slopes similar to our study sites (corresponding to the upper two layers comprised of fine regolith overlain by loose detrital cover; Sect. 2.1). Accordingly, we estimate oxidative weathering (i.e., z_{Rock}) to extend to similar depths at both study sites.

The corresponding values calculated for S_{Rock} can be compared to the inner surface area of the chambers (Table 1).

555 On average, S_{Rock} is smaller than the inner surface area of the drilled chambers, by a factor of $2.7^{+17.0}_{-2.2}$ (confidence interval includes the considered range of the weathering depth and the uncertainty of the contributing rock volume). This means that CO_2 fluxes from chambers drilled into rocks and normalized to the chamber inner surface area (Eq. 4) cannot be compared directly with topographic surface fluxes (e.g., from surface chambers), which are typically reported for soils (Oertel et al., 2016; Bond-Lamberty and Thomson, 2010). Instead, CO_2 fluxes from a drilled chamber need to be corrected by considering
560 the chamber-specific V_{Rock} and the weathering depth. The measured CO_2 fluxes (Table 5) equate to a topographic surface efflux of $\sim 541 \text{ tC km}^{-2} \text{ yr}^{-1}$ (ranging on average between $73 \text{ tC km}^{-2} \text{ yr}^{-1}$ and $1,108 \text{ tC km}^{-2} \text{ yr}^{-1}$) in the Brusquet catchment and of $\sim 425 \text{ tC km}^{-2} \text{ yr}^{-1}$ (between $43 \text{ tC km}^{-2} \text{ yr}^{-1}$ and $873 \text{ tC km}^{-2} \text{ yr}^{-1}$) in the Moulin catchment, which is roughly similar to the global mean emissions of CO_2 from soils with different land cover (Oertel et al., 2016).

Carbon fluxes from oxidative weathering can be linked to a rock mass, allowing fluxes to be interpreted in terms of
565 the overall kinetics of the oxidative weathering reactions. This is essential for theoretical carbon cycle modeling (Bolton et al., 2006; Bao et al., 2017). Following calculation of V_{Rock} , the rock mass emitting CO_2 (m_{Rock} , g) can be estimated by using an average estimate of the density of the rock grains surrounding the chambers (ρ_{Rock} , $\text{g cm}^{-3} = \text{t m}^{-3}$):

$$m_{\text{Rock}} = (V_{\text{Rock}} - V_{\text{Rock pores}}) \times \rho_{\text{Rock}} . \quad (16)$$

Considering a grain density of $2.7^{+0.02}_{-0.02} \text{ t m}^{-3}$ (Lofi et al., 2012), we find that an average rock mass of $2,955^{+10,292}_{-1,908} \text{ g}$ and
570 $2,605^{+5,651}_{-1,577} \text{ g}$ produces the CO_2 fluxes derived from chambers in the Brusquet catchment and in the Moulin catchment, respectively. To our knowledge, this allows for the first time an absolute report of weathering-derived CO_2 fluxes that are measured in real-time and in situ.

The combined quantification of CO_2 fluxes and of the corresponding rock mass undergoing oxidative weathering means that there is an opportunity for future research to include investigations of the internal surface area of the studied
575 rocks, which would allow reporting field-based CO_2 fluxes normalized to the reacting surface areas. Such normalizations are typically considered during modeling (Bao et al., 2017; Bolton et al., 2006) to acknowledge that the internal surface area can change significantly during sedimentary rock weathering (Fischer and Gaupp, 2005). Analogously to silicate weathering rates, variations in OC_{petro} and carbonate weathering rates obtained from different field and laboratory conditions may be related to the conceptualization and parametrization of the reactive surface area, which needs to be considered when
580 comparing them (Brantley et al., 2007; White and Brantley, 2003).

Table 5: Chamber-specific overview of CO₂ Excess, V_{Rock pores} and CO₂ accumulation rate (q_{plateau}), including catchment-specific summaries. Uncertainties of minima and maxima are representing the 95 % CI, whereas averages are reported with 1 SD.

Chamber identifiers		Site	CO ₂ Excess (μgC)				V _{Rock pores} (cm ³)			
<i>short</i>	<i>long</i>		Average	n	Min.	Max.	Average	n	Min.	Max.
5	B-F-5	Brusquet	222 ± 166	5	34 ⁺⁴⁴ ₋₂₄	444 ⁺⁷⁸ ₋₄₄	493 ± 279	5	120 ⁺¹⁵³ ₋₈₅	866 ⁺⁴²⁴ ₋₂₄₄
6	B-G-6	Brusquet	353 ± 267	12	64 ⁺¹³⁰ ₋₃₇	863 ⁺¹⁷⁰⁹ ₋₅₀₅	339 ± 180	12	123 ⁺²²³ ₋₆₄	666 ⁺²⁸⁶ ₋₁₈₃
7	B-H-7	Brusquet	142 ± 126	4	20 ⁺⁶⁶ ₋₁₆	336 ⁺¹³⁵² ₋₂₂₂	272 ± 182	4	71 ⁺²²⁹ ₋₅₄	537 ⁺²¹⁵⁹ ₋₃₅₄
8	B-I-8	Brusquet	261 ± 147	7	37 ⁺²⁴ ₋₁₆	450 ⁺¹⁶⁴ ₋₁₁₅	370 ± 157	7	103 ⁺⁶⁷ ₋₄₆	530 ⁺⁶⁹⁷ ₋₂₆₂
<i>Brusquet totals</i>			277 ± 221	28			365 ± 208	28		
1	M-C-1	Moulin	252 ± 150	10	10 ⁺⁵⁷ ₋₁₀	453 ⁺¹⁵² ₋₁₁₃	280 ± 122	10	38 ⁺²¹⁰ ₋₃₈	408 ⁺¹³⁷ ₋₁₀₂
2	M-A-2	Moulin	55 ± 26	4	15 ⁺¹⁷ ₋₁₁	79 ⁺¹⁴⁴ ₋₄₂	164 ± 72	4	60 ⁺⁶⁵ ₋₄₂	247 ⁺⁴⁴⁹ ₋₁₃₃
3	M-D-3	Moulin	217 ± 50	3	149 ⁺¹¹⁹ ₋₆₂	267 ⁺⁵⁹ ₋₄₆	256 ± 48	3	189 ⁺¹⁵⁰ ₋₇₉	293 ⁺⁶⁴ ₋₅₁
4	M-B-4	Moulin	296 ± 192	15	48 ⁺⁶² ₋₂₆	569 ⁺⁵⁴⁴ ₋₂₃₂	404 ± 193	15	145 ⁺¹⁸⁴ ₋₇₇	744 ⁺²³⁸ ₋₁₆₉
<i>Moulin totals</i>			245 ± 174	32			322 ± 174	32		

Chamber identifiers		Site	CO ₂ rate (μgC min ⁻¹)			
<i>short</i>	<i>long</i>		Average	n	Min.	Max.
5	B-F-5	Brusquet	6.6 ± 5.9	10	0.8 ^{+2.8} _{-0.7}	18.5 ^{+5.0} _{-1.5}
6	B-G-6	Brusquet	17.1 ± 13.5	13	2.0 ^{+0.2} _{-0.4}	39.4 ^{+4.3} _{-4.3}
7	B-H-7	Brusquet	13.8 ± 9.6	5	1.9 ^{+0.1} _{-0.3}	25.4 ^{+3.3} _{-2.4}
8	B-I-8	Brusquet	14.7 ± 7.0	8	2.6 ^{+0.3} _{-0.3}	21.5 ^{+3.1} _{-1.8}
<i>Brusquet totals</i>			13.2 ± 10.8	36		
1	M-C-1	Moulin	12.5 ± 7.4	11	1.0 ^{+0.9} _{-0.9}	21.0 ^{+1.9} _{-1.6}
2	M-A-2	Moulin	5.0 ± 3.5	6	1.2 ^{+0.3} _{-0.3}	9.4 ^{+0.5} _{-0.4}
3	M-D-3	Moulin	4.6 ± 3.1	6	0.5 ^{+0.4} _{-0.4}	9.3 ^{+1.2} _{-0.3}
4	M-B-4	Moulin	11.1 ± 8.4	18	0.9 ^{+0.1} _{-0.3}	28.0 ^{+3.0} _{-1.5}
<i>Moulin totals</i>			9.6 ± 7.7	41		

4.3 Implications for CO₂ flux measurements

585 4.3.1 Accuracy of CO₂ flux measurements

The time-dependency of carbon accumulations during the CO₂ flux measurements (Fig. 4 and 5) has provided new insights into the nature of the shallow weathering zone (Sect. 4.1 and 4.2) and has important implications for how CO₂ fluxes are

quantified. In short, changes of $p\text{CO}_2$ Chamber during the field operations are interpreted as the combination of: i) purging of CO_2 stored initially in the chamber and surrounding rock pores ($p\text{CO}_2$ Rock); and ii) the real-time production of CO_2 from oxidative weathering. At the start of a CO_2 flux measurement, CO_2 accumulations have important contributions from i), which led previous studies to use the later repeats (q_4 to $q_n \geq 6$) to quantify ii) (Soulet et al., 2018, 2021; Roylands et al., 2022). Here, longer measurements at each chamber allow us to explore this in more detail.

The time it takes for the CO_2 accumulation rates to decline and stabilize within the 95 % confidence interval of the q_{Plateau} value derived from fitting CO_2 accumulation rates over time (Eq. 9) is ~ 90 min corresponding to ~ 10 repeats (Fig. 5). This implies that treating only the first 3 repeats of a measurement as combined signals of purging and production of CO_2 , as done previously in similar studies (Roylands et al., 2022; Soulet et al., 2021, 2018), returns a greater flux than q_{Plateau} . However, the overestimate is modest: the average accumulation rate of the measured repeats 4 - 6 is ~ 15 % higher than the q_{Plateau} value (Fig. 10A). This is true for the entire data set, including stabilized and extrapolated measurements, and for the site-specific samples. The relative offset is constant irrespective of the overall size of the CO_2 accumulation (Fig. 10A), which means that flux data including non-plateaued accumulations can be corrected. It also means that any link between CO_2 flux and measured environmental variables is robust (Roylands et al., 2022; Soulet et al., 2021). When taking the average of the measured repeats 6 - 8 (Fig. 10B), the value is ~ 7 % higher than q_{Plateau} .

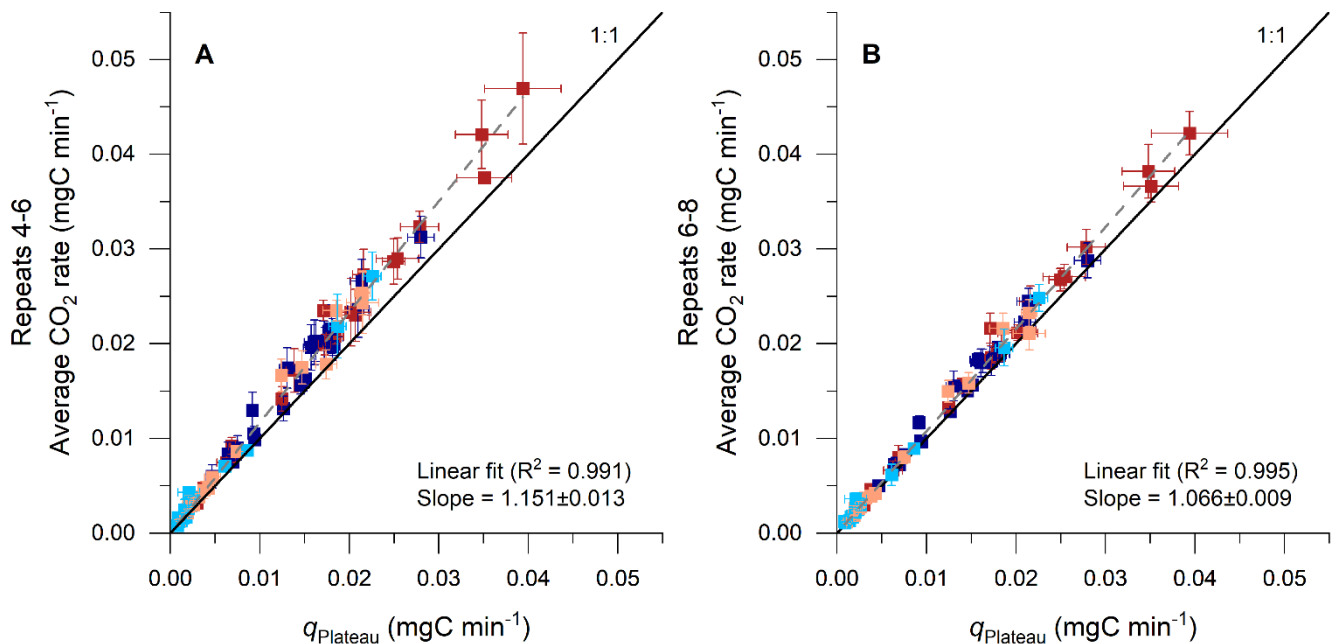


Figure 10: Comparison of CO_2 fluxes determined by using the average of repeated accumulation rates and by an exponential fitting model. Results from the proposed model are given on the x-axis (q_{Plateau} , Eq. 9; error bars: 95 % CI) and are compared with the averages of the repeats 4 - 6 (Panel A) and of the repeats 6 - 8 (Panel B) on the y-axis (error bars: 2 SD), alongside a linear regression and a 1:1 line for reference. Red colors indicate samples from the Brusquet catchment (stabilized: dark, extrapolated fitting: light; Sect. 4.1.1), and blue colors indicate samples from the Moulin catchment (stabilized: dark, extrapolated fitting: light).

610 4.3.2 Reporting CO₂ flux as a function of temperature

Recent research has highlighted that temperature controls the release of CO₂ from chambers drilled into the shallow weathering zone of sedimentary rocks (Soulet et al., 2021), with an exponential response:

$$F = F_0 \times \exp(\gamma T), \quad (17)$$

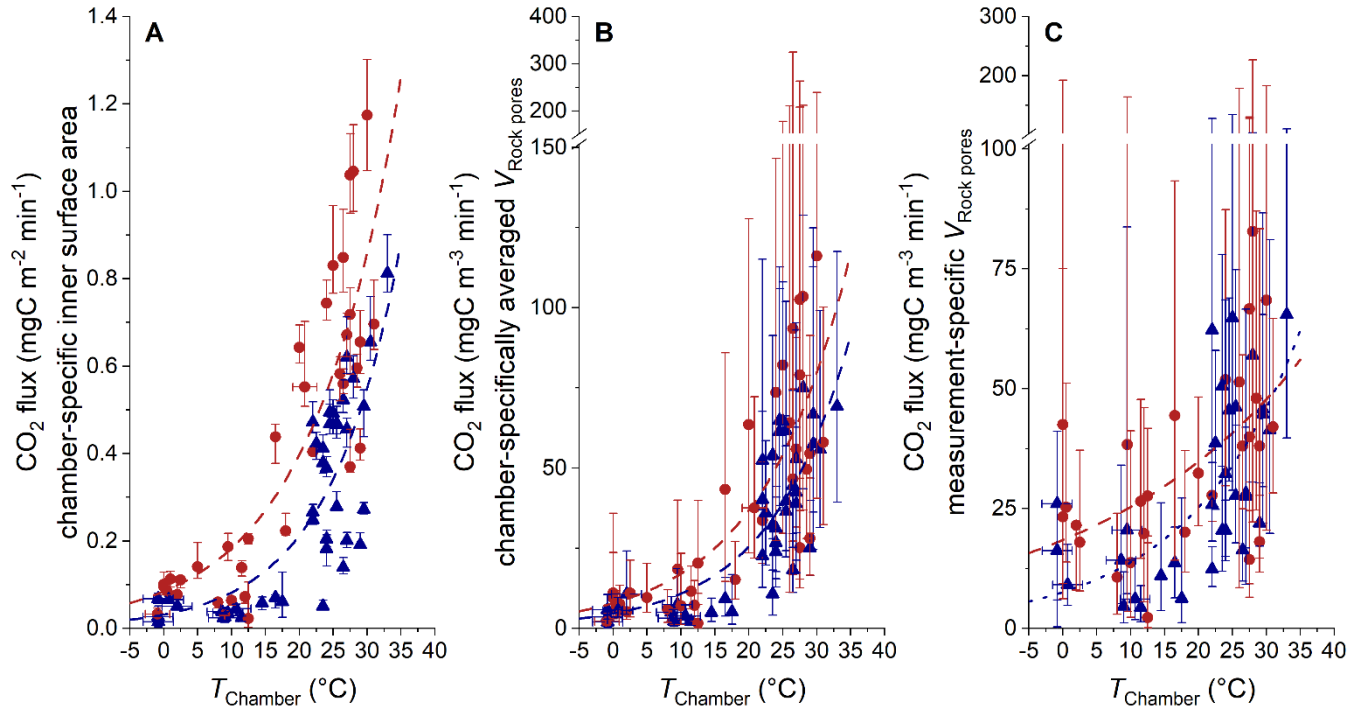
615 where F is the CO₂ flux (mgC m⁻² d⁻¹, using the chamber-specific inner surface area), T is the temperature (°C), F_0 is the CO₂ flux at 0 °C and γ is the growth rate parameter (°C⁻¹) that is derived from an exponential model. For the oxidation of marls, Soulet et al. (2021) found a value for γ of 0.070 ± 0.007 °C⁻¹ (\pm standard error) considering five different chambers independent of their F_0 values, based on daily-averaged chamber temperatures. Across differences in the hydrological setting of these chambers, F_0 values ranged from 35 ± 7 mgC m⁻² d⁻¹ to 626 ± 113 mgC m⁻² d⁻¹ with the lowest CO₂ fluxes in close proximity to a riverbed (Soulet et al., 2021).

620 Here, at different installation sites, we find a similar exponential response of CO₂ release to temperature with γ values of 0.065 ± 0.012 °C⁻¹ (Brusquet) and 0.067 ± 0.018 °C⁻¹ (Moulin). However, using an hourly resolution for the chamber temperature (Fig. 11A) returns higher γ values (0.077 ± 0.013 °C⁻¹ at Brusquet; 0.085 ± 0.016 °C⁻¹ at Moulin). This increase in γ can be explained by an instantaneous response of weathering reactions to in situ temperature changes, and fits to the observation that CO₂ fluxes increased over a few hours alongside increases of chamber temperature for chambers
625 visited twice a day (Appendix F). Overall, this observation highlights the importance of considering the in situ environmental conditions with a high temporal resolution (Sect. 3.1).

Changes in temperature also coincide with changes in the diffusive processes in the rocks surrounding a chamber (Sect. 4.1). To differentiate changes in the diffusive framework from the CO₂ production at a given temperature (i.e., weathering kinetics), the CO₂ fluxes can be normalized to $V_{\text{Rock pores}}$, which is representative for the contributing amount of
630 rock grains undergoing oxidation (Sect. 4.2). Since the observed CO₂ fluxes range by a factor of ~ 18.2 , while values of $V_{\text{Rock pores}}$ exhibit a lower range of a factor of ~ 5.9 (Table 5), this normalization does not diminish the importance of the temperature control on the CO₂ release (Fig. 11C). However, due to large measurement-specific uncertainties that are associated with the calculation of $V_{\text{Rock pores}}$, a full assessment of whether higher chamber-derived CO₂ fluxes at higher temperatures are partly a result of greater contributing rock volumes is hindered.

635 Despite the similarities of the topography, hydrology, erosion rates (Fig. 1 and 2) and $V_{\text{Rock pores}}$ (Fig. 7 and 8), we find site-specific differences in the bulk CO₂ production at a given temperature, which may be linked to differences in the source of carbon associated with the different rock types outcropping in the Brusquet catchment (black shales; $F_0 = 122.2 \pm 41.3$ mgC m⁻² d⁻¹) and in the Moulin catchment (marls; $F_0 = 45.6 \pm 20.3$ mgC m⁻² d⁻¹). To better understand these different weathering fluxes, future research is needed to assess the carbon source(s) and the response of the weathering
640 reactions to changes in temperature at both study sites in more detail, for instance, by studying the chemical composition of the rocks (i.e., contents of OC_{petro}, carbonates and sulfides) alongside the radiocarbon and stable carbon isotope composition

of the released CO₂, analogously to previous research in the neighboring Laval catchment (Soulet et al., 2018, 2021) and in the Waiapu catchment in New Zealand (Roylands et al., 2022).



645 **Figure 11: Comparison of CO₂ fluxes with different normalizations and chamber temperature. Panel A: normalization to the**
chamber-specific inner surface area (Table 1) (including the 95 % CI of q_{Plateau}). Panel B: normalization to chamber-specifically
averaged $V_{\text{Rock pores}}$ (Table 5) (including the combined uncertainty of q_{Plateau} and the averaged 95 % CI of $V_{\text{Rock pores}}$). Panel C:
normalization to measurement-specific $V_{\text{Rock pores}}$ (including the combined uncertainty of q_{Plateau} and the measurement-specific
650 **95 % CI of $V_{\text{Rock pores}}$). Estimated temperatures are indicated by accompanying error bars (RMSE). Colors indicate the site of**
measurement (Brusquet: red circles, Moulin: blue triangles).

4.4 Linking CO₂ and O₂ fluxes

The O₂ consumption in the weathering zone provides a tool for investigating the kinetics of sedimentary rock weathering (Tune et al., 2020, 2023), analogously to previous research on soils (Hicks Pries et al., 2020; Angert et al., 2015; Sánchez-Cañete et al., 2018). Overall, $p\text{O}_2$ Chamber values in the Brusquet catchment and in the Moulin catchment were similar or lower
655 than the O₂ concentration of the atmosphere, confirming that the weathering zones are sinks of oxygen. The variation of $p\text{O}_2$ Chamber over time coincides with a variation in temperature within the chambers (Fig. 12A), with roughly similar relationships for both study sites. This observation fits to the recently proposed importance of temperature controlling oxidative weathering kinetics (Soulet et al., 2021). However, due to a limited number of samples and a large measurement uncertainty, neither chamber-specific differences nor the impact of precipitation on $p\text{O}_2$ Chamber can be evaluated accurately.

660 The observed $p\text{O}_2$ Chamber values can be used to calculate a diffusive flux of O₂ between the chamber, connected rock pores and the atmosphere (Eq. 7 and 8). This is based on the insights into the diffusive processes of the chambers and the

connected rock space that come from the CO₂ measurements (Sect. 2.7 and 4.1) (Appendix B). Previous work on porous media has established that the effective diffusivities of CO₂ and O₂ are impacted in a similar way by the structure of the air-filled pore space (Millington, 1959; Penman, 1940; Angert et al., 2015), which allows determination of the effective
665 diffusivity of O₂ from that of CO₂ in the shallow weathering zone.

The calculated O₂ fluxes are representative of the same rock volume that is releasing CO₂, which also means that a report of absolute fluxes is possible (Sect. 4.2). Altogether, the chamber-specific O₂ exchange rate in the Brusquet catchment and the Moulin catchment range between zero within uncertainty ($0.42^{+0.58}_{-0.88}$ μmol O₂ min⁻¹) to a maximum consumption of O₂ of $-16.33^{+5.72}_{-7.75}$ μmol O₂ min⁻¹, with increasing O₂ consumption with increasing temperature (Fig. 12B). The O₂ fluxes
670 have a greater relative uncertainty compared to the pO₂ gradient because they include the measurement-specific diffusivity.

The O₂ flux into the chambers and their connected rock pores can be compared with the CO₂ flux from this space (Fig. 12C). At 20 °C, an O₂ consumption rate of ~ -8.7 μmol O₂ min⁻¹ coincides with an average CO₂ accumulation rate of ~ 1.1 μmol CO₂ min⁻¹ in the Brusquet catchment and of ~ 0.6 μmol CO₂ min⁻¹ in the Moulin catchment. This is an average ratio of ~ 1 mol O₂ : 0.1 mol CO₂. This field-based molar ratio of O₂ consumption and CO₂ release is significantly lower than
675 the theoretical ratio of weathering reactions describing the oxidation of sedimentary rocks. For example, the oxidation of OC_{petro} is theoretically described by a ratio of 1 mol O₂ : 1 mol CO₂ (Petsch, 2014). In addition, the oxidation of pyrite minerals coupled to the dissolution of carbonates is theoretically characterized by a ratio of up to 1.875 mol O₂ : 1 mol CO₂ if the CO₂ release occurs in situ (Torres et al., 2014; Soulet et al., 2021). To investigate this discrepancy, here we discuss several mechanisms that could influence the consumption of O₂ and the release of CO₂ in the shallow weathering zone.
680 In addition to OC_{petro} and pyrite minerals, other minerals, such as illite, chlorite, and ankerite, can be a sink of oxygen during the weathering of sedimentary rocks (Brantley et al., 2013; Sullivan et al., 2016). However, in settings where pyrite minerals are present, the chemical weathering of these other ferrous iron bearing minerals progresses relatively slowly and advances only more rapidly following the complete oxidation of pyrite minerals (Gu et al., 2020a, b). Accordingly, pyrite minerals should be the dominating inorganic O₂ sink at the two study sites.

It has been previously suggested that the oxidation of OC_{petro} progresses in a stepwise manner, with the formation of oxygenated compounds of organic matter prior to the release of CO₂ (Chang and Berner, 1999), typically resulting in an increase of the relative oxygen content of OC_{petro} during chemical weathering (Petsch, 2014; Tamamura et al., 2015; Longbottom and Hockaday, 2019). If the oxidation of OC_{petro} progresses more rapidly than the separate process of CO₂ release from oxygenated OC_{petro} in the Draix-Bléone observatory, this could partly explain the lower ratio of CO₂ released
690 compared to the O₂ uptake. However, for rocks exposed in rapidly eroding terrains in the Draix-Bléone observatory, previous studies did not find a significant effect of weathering on the chemical composition of OC_{petro}, despite a decrease in the quantities of OC_{petro} and pyrite minerals (Graz et al., 2011; Copard et al., 2006). Thus, it seems unlikely that the oxidation of OC_{petro} at both study sites deviates notably from the theoretical stoichiometry mentioned above.

Furthermore, if the sulfuric acid derived from the oxidation of pyrite minerals interacts with silicate minerals (Bufe
695 et al., 2021; Blattmann et al., 2019), this would lead to O₂ consumption but no CO₂ release. In addition, sulfuric acid could

interact with OC_{petro} and be neutralized, yet the vast majority of OC_{petro} is typically made of kerogen, which is resistant to acid hydrolysis, and only minor amounts of more labile organic matter can be prone to this type of degradation (Killops and Killops, 2005; Petsch, 2014; Seifert et al., 2011; Włodarczyk et al., 2018).

Another explanation may involve the lateral transport of CO_2 as part of the dissolved load, lowering the gaseous release of carbon. The oxidation of OC_{petro} and pyrite minerals coupled to the dissolution of carbonates occur in a humid weathering zone (Fig. 3), where CO_2 may be incorporated into the dissolved inorganic carbon pool (Torres et al., 2014; Soulet et al., 2021; Roylands et al., 2022; Bao et al., 2017). A recent study has quantified the export of DIC using the molar ratio of O_2 and CO_2 fluxes for sedimentary rocks undergoing weathering below a forested hillslope (Tune et al., 2023, 2020). There, carbon is sourced from soils, roots and OC_{petro} , with an absence of an inorganic carbon source and of pyrite minerals. If a part of the CO_2 from oxidative weathering is exported as DIC in the Brusquet and the Moulin catchments, this would raise the observed O_2 consumption to CO_2 release ratio, and would have to do so by a factor in the range of ~ 4 and ~ 15 . This is worthy of future research towards understanding O_2 consumption in the weathering zone. Here, a more accurate quantification is hindered because the proportions of inorganic carbon release versus organic carbon release (which derive from weathering reactions with a different stoichiometry as described above) are unknown. This again calls for future work to assess the carbon sources in more detail.

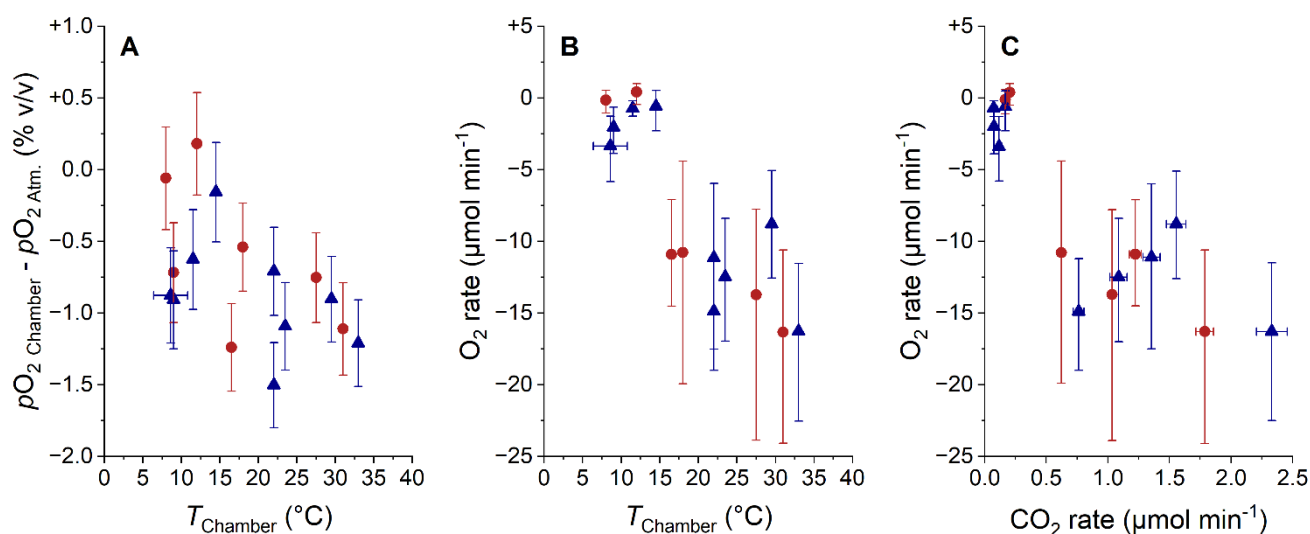


Figure 12: Comparison of $pO_2 \text{ Chamber}$ (Panel A, normalized to atmospheric pO_2 , error bars: RMSE) and of O_2 consumption rate (Panel B, error bars: 95 % CI) with chamber temperature, and comparison of O_2 consumption rate with CO_2 production rate (Panel C, error bars: 95 % CI). The origin of samples is indicated with red circles for the Brusquet catchment and blue triangles for the Moulin catchment. Estimated temperatures are indicated by accompanying error bars (RMSE).

Overall, we have developed the tools needed to quantify the production or consumption, storage and movement of CO_2 and O_2 in the near-surface of rocks undergoing weathering (Appendix B). If combined, for example, with surface chambers (for gaseous exchange) and boreholes extending below the oxidation front (profiling gaseous and dissolved

720 processes) (Tune et al., 2020; Tokunaga et al., 2016), alongside radiocarbon and stable carbon isotope analyses (for partitioning the weathering reactions) (Soulet et al., 2021; Roylands et al., 2022; Keller and Bacon, 1998; Tune et al., 2023), the cycling of carbon and oxygen in the total critical zone and its environmental controls could be investigated comprehensively. Using drilled chambers benefits investigations using the gradient method for profiles of gas concentrations, because with the approach suggested here the diffusivity measures can be determined in situ and in real-time, 725 which are otherwise typically estimated (Tune et al., 2020; Maier and Schack-Kirchner, 2014; Keller and Bacon, 1998; Tokunaga et al., 2016). Furthermore, by assessing the release and movement of nitrous oxide from the subsurface (Wan et al., 2021), an overall greenhouse gas budget could be developed for sedimentary rocks undergoing weathering. This would be especially valuable for sites with a thin soil cover, which typically dominate more widespread terrains at lower slopes (Milodowski et al., 2015; Heimsath et al., 2012). There, the additional, modern carbon pool complicates the disentangling of 730 biogeochemical processes and the corresponding source-specific CO₂ and O₂ fluxes (Tune et al., 2020; Keller and Bacon, 1998; Longbottom and Hockaday, 2019; Hemingway et al., 2018; Copard et al., 2006; Tune et al., 2023).

5 Conclusions

This study has further developed and assessed methods for in situ constraints on the release of CO₂ and the consumption of O₂ during oxidative weathering of exposed sedimentary rocks. Our new method framework allows for both accurate 735 quantification of weathering fluxes over hourly to daily timescales, while also constraining diffusive processes in the shallow weathering zone. At two sites of the Draix-Bléone observatory (France), accumulation chambers were installed by drilling holes directly into rocks undergoing weathering in the Brusquet catchment (black shales) and in the Moulin catchment (marls). At each site, using an array of 4 chambers, measurements of $p\text{CO}_{2\text{ Rock}}$ and CO₂ fluxes were carried out alongside $p\text{O}_{2\text{ Rock}}$ measurements during six fieldtrips over one year.

740 We find that during a single visit to a chamber, the accumulation rates decline over a few measurement cycles, before reaching a stable CO₂ accumulation rate. This pattern is consistent across the fieldtrips and can be described by an exponential model. To explain these observations, we outline a framework which considers the measured CO₂ accumulation as a combination of the real-time production during weathering, plus the release of excess CO₂ built up in pore space surrounding the chambers. By doing so, we can assess the rock pore volume and rock mass that produce CO₂. For the first 745 time, this allows an absolute report of rock-derived CO₂ fluxes measured in situ and in real-time, providing input data for future studies modeling the chemical weathering of sedimentary rocks. The assessment of contributing rock pore space allows us also to normalize the fluxes to an outcrop surface area, enabling comparison of the weathering fluxes at the study sites to other rock types and soils across different terrains and climates. Furthermore, by studying the accumulation of CO₂ in a chamber and the connected rock pore space over time, the diffusivity of gases in the shallow weathering zone and its 750 environmental controls are investigated, including an absolute, in situ determination of the diffusion coefficients.

In addition to these insights into the CO₂ release, *p*O₂ values for the studied rocks are presented and used together with the quantification of the diffusive processes in the weathering zone to calculate O₂ fluxes. It is shown that the consumption of O₂ co-varies with changes in the emission of CO₂ over time, which are driven by changes in temperature. However, the O₂ fluxes indicate significantly greater oxidative weathering rates compared to the CO₂ fluxes. We suggest this discrepancy results of: i) export of inorganic carbon by the dissolved load of percolating waters lowering the effective release of gaseous CO₂; and ii) silicate weathering by sulfuric acid as a sink of O₂.

A site-specific difference in the magnitude of CO₂ emissions at the two study sites cannot be explained by differences in the lithological properties influencing the diffusion of gas within the rock space surrounding the chambers as both study sites have similar characteristics, which is evidenced by diffusivity measures changing similarly alongside temperature and precipitation. This finding suggests that differences in the source of carbon are the main reason for the observed CO₂ flux differences, providing an opportunity for future research to investigate the control of the chemical composition of the rocks (i.e., contents of OC_{petro}, carbonates and sulfides) on the CO₂ flux size.

Appendices

Appendix A - Modeling chamber temperatures

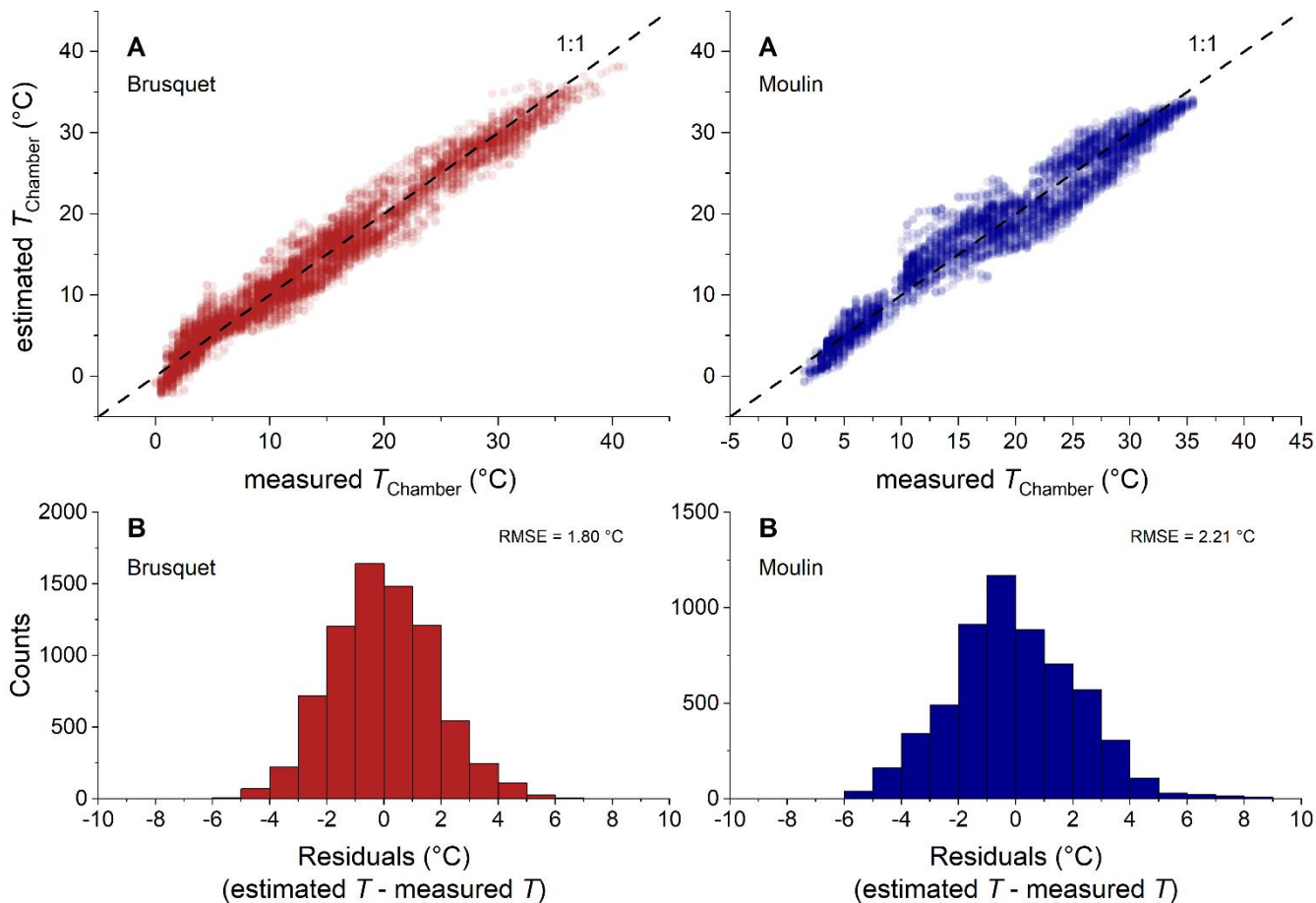
To fill the gaps in the direct chamber temperature measurements, we use air temperatures from a local weather station as a proxy by modifying a framework that describes soil temperatures by, amongst other variables, air temperature (Liang et al., 2014). The approach combines measured air temperatures with a Fourier-fitted function that describes the daily average temperature inside the rock chambers by weighting averaged air temperatures by the fractional duration of daylight (*L*) at the latitude of the Draix-Bléone observatory. In more detail, we estimate the current chamber temperature T_{Chamber} (°C) at an hourly resolution as follows:

$$T_{\text{Chamber}} = T_{\text{mean}} \times \text{coeff}_A + (T_{\text{Air-6h}} - T_{\text{mean}}) \times \text{coeff}_B, \quad (\text{A1})$$

where $T_{\text{Air-6h}}$ is the hourly air temperature (°C) from nearby meteorological stations (Draix-Bléone Observatory, 2015) delayed by 6 hours, coeff_A and coeff_B are site-specific fitting coefficients, and T_{mean} (°C) is the long-term trend of rock temperature described by:

$$T_{\text{mean}} = \text{coeff}_{C1} + \text{coeff}_{C2} \times \cos(\text{coeff}_{C3} \times T_{\text{Air,7d}} \times L) + \text{coeff}_{C4} \times \sin(\text{coeff}_{C3} \times T_{\text{Air,7d}} \times L), \quad (\text{A2})$$

where coeff_{C1} to coeff_{C4} are site-specific fitting coefficients (Table A1) in a 1st order Fourier-model, and $T_{\text{Air,7d}}$ (°C) is the 7-day average of the past air temperatures at hourly resolution. Using the site-specific air temperatures, this approach simulates T_{Chamber} well, with a root-mean-square error (RMSE) of 1.8 °C for the Brusquet catchment and 2.2 °C for the Moulin catchment (Fig. A1).



780

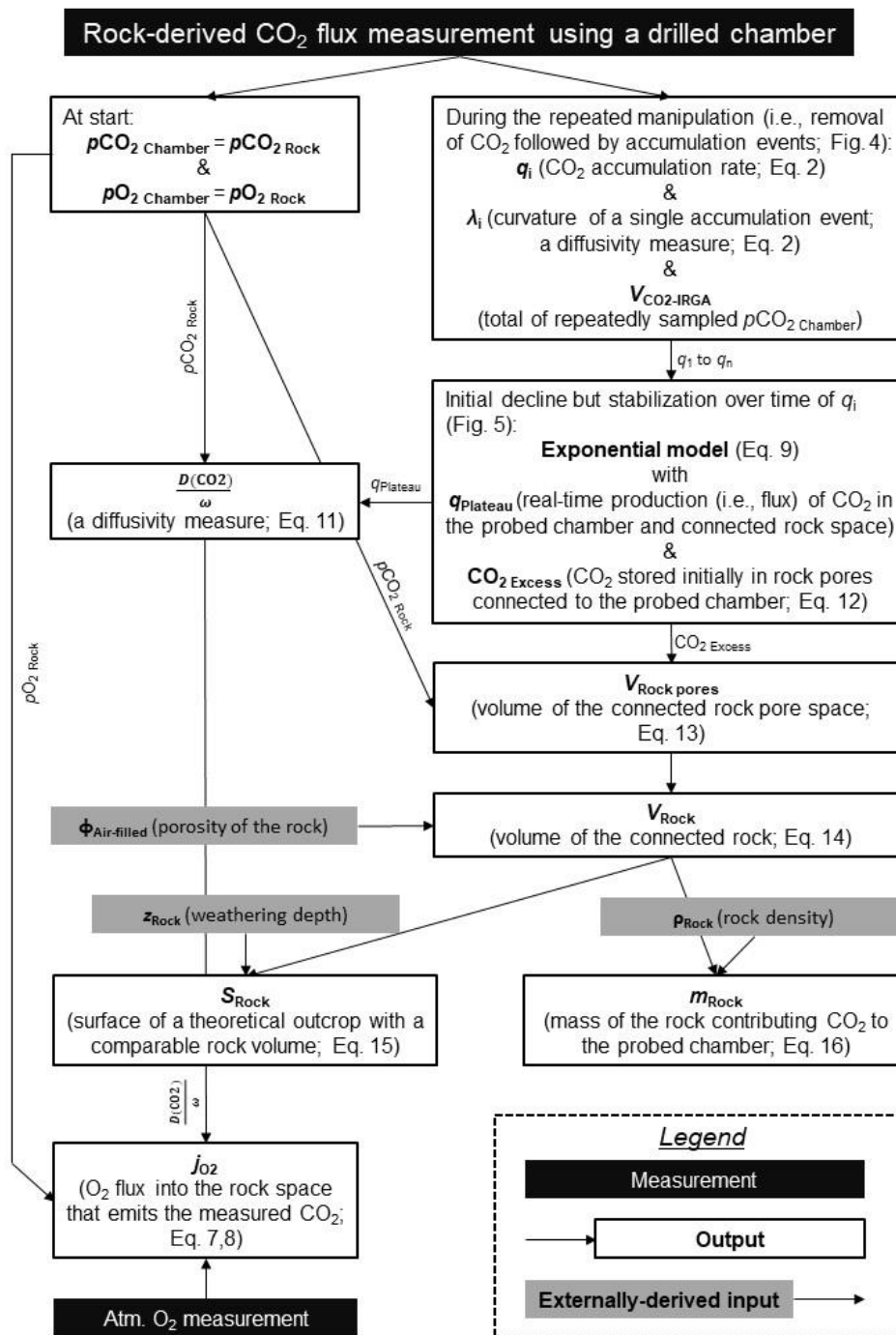
Figure A1: Panels A: comparison of chamber temperatures measured and estimated by a modeling framework based on air temperature and the fractional duration of daylight at the latitude of the Draix-Bléone observatory at hourly resolution for the Brusquet catchment (red) and the Moulin catchment (blue), which agree with a 1:1 relation (dashed line). Panels B: normally distributed residuals between the measured temperatures and the modeling framework.

785

Table A1: Overview of site-specific fitting coefficients used for modeling chamber temperatures based on air temperature and fractional duration of daylight (Eq. A1 and A2) and details of the goodness of the fitting model based on comparisons to measured chamber temperatures with hourly and daily resolution.

Site	R^2	p-value	n	RMSE (hourly) (°C)	RMSE (daily) (°C)	coeff _A	coeff _B	coeff _{C1}	coeff _{C2}	coeff _{C3}	coeff _{C4}
Brusquet	0.96	<0.001	7,392	1.80	1.58	1.147	0.361	0.408	2.364	0.080	30.106
Moulin	0.94	<0.001	5,664	2.21	1.99	1.222	0.298	0.362	2.074	0.093	26.407

Appendix B - Data-flow diagram for chamber-based CO₂ and O₂ flux measurements



790 **Figure B1:** Central data-flow for the new approach developed in this study to quantify the diffusive exchange of CO₂ and O₂ during shallow rock weathering based on real-time measurements using drilled headspace chambers.

Appendix C - Linear regression of $p\text{CO}_2\text{Rock}$ and CO_2 accumulation rates

795 **Table C1: Details of linear regressions comparing measurement-specific values of $p\text{CO}_2\text{Rock}$ and CO_2 accumulation (based on repeats 6 - 8) (with $p\text{CO}_2$ (ppmv) = $a_1 \times \text{CO}_2$ rate ($\mu\text{gC min}^{-1}$) + a_2) including the standard errors of the fitting parameters. Differentiations into “dry” and “wet” samples are based on a threshold of a cumulative precipitation of 5 mm over 3 days prior to the measurement. Both sites have similar linear regressions with overlapping standard errors.**

Data set	a_1	a_2	R^2	p-value	n
all	55.1 ± 5.1	848.7 ± 83.5	0.69	<0.001	55
<i>Brusquet</i>	55.0 ± 6.3	741.6 ± 120.5	0.77	<0.001	25
<i>Moulin</i>	61.1 ± 8.5	872.5 ± 117.0	0.64	<0.001	30
all - dry	59.1 ± 6.4	664.3 ± 122.2	0.75	<0.001	31
all - wet	61.0 ± 8.3	948.7 ± 101.0	0.71	<0.001	24

Appendix D - Linear regression of diffusivity measures

800 **Table D1: Details of linear regressions comparing the diffusivity measures $\frac{D(\text{CO}_2)}{\omega}$ and λ (with $\frac{D(\text{CO}_2)}{\omega}$ ($\text{cm}^3 \text{min}^{-1}$) = $b_1 \times \lambda$ (min^{-1}) + b_2) including the standard errors of the fitting parameters. Differentiations into “dry” and “wet” samples are based on a threshold of a cumulative precipitation of 5 mm over 3 days prior to the measurement. The regressions are based on using the average values from the repeats 6 - 8 of the flux measurements, which is typically close to stabilization of the CO_2 accumulation rate, because a significant number of the measurements was limited to 8 repeats. Both sites have comparable linear regressions with overlapping standard errors.**

Data set	b_1	b_2	R^2	p-value	n
all	163.4 ± 13.2	-1.13 ± 2.25	0.74	<0.001	55
<i>Brusquet</i>	162.1 ± 13.9	-1.54 ± 2.67	0.86	<0.001	25
<i>Moulin</i>	170.4 ± 24.0	-1.57 ± 3.61	0.64	<0.001	30
all - dry	151.4 ± 18.5	2.25 ± 3.58	0.71	<0.001	31
all - wet	157.2 ± 22.9	-1.94 ± 3.13	0.68	<0.001	24

805 Appendix E - Different diffusion pathways of a closed versus manipulated chamber

The diffusion pathways of a closed chamber differ from that of a manipulated chamber. During a flux measurement, CO_2 , which is released from a rock grain undergoing oxidative weathering into the pore space, moves via diffusion along a concentration gradient, which is initiated by lowering repeatedly the $p\text{CO}_2\text{Chamber}$ to a near-atmospheric level (Soulet et al., 2018), from the rock pores towards the manipulated chamber if they are connected more effectively to the chamber than to the rock-atmosphere boundary. In contrast, without a sampling system acting as the receiving reservoir, rock-derived CO_2 travels along the concentration gradient towards the atmosphere. In the latter scenario, rock pores that contribute CO_2 during a flux measurement to a chamber either contribute the CO_2 via diffusion directly to the atmosphere (without a pathway through the chamber) or through the chamber towards the atmosphere.

Appendix F - Repeated CO₂ flux measurements on the same date

815 On four visits, a chamber was measured twice a day and the observed CO₂ release was higher in the afternoon than in the morning, coinciding with an increase of the chamber temperature: for chamber 5 at the Brusquet site, q_{plateau} increased from 1.1 $\mu\text{gC min}^{-1}$ to 3.8 $\mu\text{gC min}^{-1}$ and from 2.6 $\mu\text{gC min}^{-1}$ to 4.7 $\mu\text{gC min}^{-1}$ coinciding with temperature increases from -0.9 °C to 1.0 °C and from 2.0 °C to 5.0 °C, respectively; for chamber 4 at the Moulin site, q_{plateau} increased from 14.6 $\mu\text{gC min}^{-1}$ to 18.0 $\mu\text{gC min}^{-1}$ and from 16.3 $\mu\text{gC min}^{-1}$ to 21.4 $\mu\text{gC min}^{-1}$ coinciding with temperature increases from 22.5 °C to 26.5 °C and
820 from 22.0 °C to 27.0 °C, respectively.

Data availability

All data supporting the findings of this study can be found in supplementary tables.

Author contribution

The research was conceptualized by TR, with help from RGH and ELM. The main methods were designed by TR, with help
825 from RGH, GS, MHG and ELM. Field-based and laboratory geochemical measurements were led by TR, with contributions from MHG, RGH, SK, MD and FN, and climate data and aerial imagery were provided by SK and CLB. TR led the formal analysis, investigation, data visualization and writing of the original draft, under the supervision of RGH and ELM. All authors contributed to subsequent review and editing, led by TR, RGH, ELM and GS. Funding was acquired by RGH, TR and MHG.

830 Competing interests

The authors declare that they have no conflict of interest.

Acknowledgements

This work was supported by the European Research Council (Starting Grant to RGH, ROC-CO₂ project, grant 678779). Analytical work was also supported in part by the Natural Environment Research Council (NERC, UK; NEIF Radiocarbon
835 Grant to TR, RGH and MHG, grant 2201.1019).

References

Angert, A., Yakir, D., Rodeghiero, M., Preisler, Y., Davidson, E. A., and Weiner, T.: Using O₂ to study the relationships between soil CO₂ efflux and soil respiration, *Biogeosciences*, 12, 2089–2099, <https://doi.org/10.5194/bg-12-2089-2015>,

2015.

- 840 Antoine, P., Giraud, A., Meunier, M., and Van Asch, T.: Geological and geotechnical properties of the “Terres Noires” in southeastern France: Weathering, erosion, solid transport and instability, *Eng. Geol.*, 40, 223–234, [https://doi.org/10.1016/0013-7952\(95\)00053-4](https://doi.org/10.1016/0013-7952(95)00053-4), 1995.
- Ariagno, C., Le Bouteiller, C., van der Beek, P., and Klotz, S.: Sediment export in marly badland catchments modulated by frost-cracking intensity, Draix–Bléone Critical Zone Observatory, SE France, *Earth Surf. Dyn.*, 10, 81–96,
- 845 <https://doi.org/10.5194/esurf-10-81-2022>, 2022.
- Ariagno, C., Pasquet, S., Le Bouteiller, C., van der Beek, P., and Klotz, S.: Seasonal dynamics of marly badlands illustrated by field records of hillslope regolith properties, Draix–Bléone Critical Zone Observatory, South-East France, *Earth Surf. Process. Landforms*, 1–14, <https://doi.org/10.1002/esp.5564>, 2023.
- Bao, Z., Haberer, C. M., Maier, U., Amos, R. T., Blowes, D. W., and Grathwohl, P.: Modeling controls on the chemical
- 850 weathering of marine mudrocks from the Middle Jurassic in Southern Germany, *Chem. Geol.*, 459, 1–12, <https://doi.org/10.1016/j.chemgeo.2017.03.021>, 2017.
- Bechet, J., Duc, J., Jaboyedoff, M., Loye, A., and Mathys, N.: Erosion processes in black marl soils at the millimetre scale: preliminary insights from an analogous model, *Hydrol. Earth Syst. Sci.*, 19, 1849–1855, <https://doi.org/10.5194/hess-19-1849-2015>, 2015.
- 855 Bechet, J., Duc, J., Loye, A., Jaboyedoff, M., Mathys, N., Malet, J.-P., Klotz, S., Le Bouteiller, C., Rudaz, B., and Travelletti, J.: Detection of seasonal cycles of erosion processes in a black marl gully from a time series of high-resolution digital elevation models (DEMs), *Earth Surf. Dyn.*, 4, 781–798, <https://doi.org/10.5194/esurf-4-781-2016>, 2016.
- Berner, E. K. and Berner, R. A.: *Global environment: Water, Air, and Geochemical cycles*, 2nd ed., Princeton University Press, New Jersey, USA., 2012.
- 860 Berner, R. A.: A New Look at the Long-term Carbon Cycle, *GSA Today*, 9, 1–6, 1999.
- Blattmann, T. M., Wang, S.-L., Lupker, M., Märki, L., Haghypour, N., Wacker, L., Chung, L.-H., Bernasconi, S. M., Plötze, M., and Eglinton, T. I.: Sulphuric acid-mediated weathering on Taiwan buffers geological atmospheric carbon sinks, *Sci. Rep.*, 9, 2945, <https://doi.org/10.1038/s41598-019-39272-5>, 2019.
- Bolton, E. W., Berner, R. A., and Petsch, S. T.: The Weathering of Sedimentary Organic Matter as a Control on Atmospheric
- 865 O₂: II. Theoretical Modeling, *Am. J. Sci.*, 306, 575–615, <https://doi.org/10.2475/08.2006.01>, 2006.
- Bond-Lamberty, B. and Thomson, A.: A global database of soil respiration data, *Biogeosciences*, 7, 1915–1926, <https://doi.org/10.5194/bg-7-1915-2010>, 2010.
- Le Bouteiller, C., Chambon, G., Naaim-Bouvet, F., and Mathys, N.: Hydraulics and rheology of natural hyperconcentrated flows from Draix-Bleone observatory, French Alps, *J. Hydraul. Res.*, 59, 181–195,
- 870 <https://doi.org/10.1080/00221686.2020.1744750>, 2021.
- Brantley, S. L., Goldhaber, M. B., and Ragnarsdottir, K. V.: Crossing Disciplines and Scales to Understand the Critical Zone, *Elements*, 3, 307–314, <https://doi.org/10.2113/gselements.3.5.307>, 2007.

- Brantley, S. L., Holleran, M. E., Jin, L., and Bazilevskaya, E.: Probing deep weathering in the Shale Hills Critical Zone Observatory, Pennsylvania (USA): the hypothesis of nested chemical reaction fronts in the subsurface, *Earth Surf. Process. Landforms*, 38, 1280–1298, <https://doi.org/10.1002/esp.3415>, 2013.
- 875 Bufo, A., Hovius, N., Emberson, R., Caves Rügenstein, J. K., Galy, A., Hassenruck-Gudipati, H. J., and Chang, J.-M.: Co-variation of silicate, carbonate and sulfide weathering drives CO₂ release with erosion, *Nat. Geosci.*, 14, 211–216, <https://doi.org/10.1038/s41561-021-00714-3>, 2021.
- Burke, A., Present, T. M., Paris, G., Rae, E. C. M., Sandilands, B. H., Gaillardet, J., Peucker-Ehrenbrink, B., Fischer, W. W.,
880 McClelland, J. W., Spencer, R. G. M., Voss, B. M., and Adkins, J. F.: Sulfur isotopes in rivers: Insights into global weathering budgets, pyrite oxidation, and the modern sulfur cycle, *Earth Planet. Sci. Lett.*, 496, 168–177, <https://doi.org/10.1016/j.epsl.2018.05.022>, 2018.
- Calmels, D., Gaillardet, J., Brenot, A., and France-Lanord, C.: Sustained sulfide oxidation by physical erosion processes in the Mackenzie River basin: Climatic perspectives, *Geology*, 35, 1003–1006, <https://doi.org/10.1130/G24132A.1>, 2007.
- 885 Carriere, A., Le Bouteiller, C., Tucker, G. E., Klotz, S., and Naaim, M.: Impact of vegetation on erosion: Insights from the calibration and test of a landscape evolution model in alpine badland catchments, *Earth Surf. Process. Landforms*, 45, 1085–1099, <https://doi.org/10.1002/esp.4741>, 2020.
- Chang, S. and Berner, R. A.: Coal weathering and the geochemical carbon cycle, *Geochim. Cosmochim. Acta*, 63, 3301–3310, [https://doi.org/10.1016/S0016-7037\(99\)00252-5](https://doi.org/10.1016/S0016-7037(99)00252-5), 1999.
- 890 Copard, Y., Di-Giovanni, C., Martaud, T., Albéric, P., and Olivier, J.-E.: Using Rock-Eval 6 pyrolysis for tracking fossil organic carbon in modern environments: implications for the roles of erosion and weathering, *Earth Surf. Process. Landforms*, 31, 135–153, <https://doi.org/10.1002/esp.1319>, 2006.
- Cras, A., Marc, V., and Travi, Y.: Hydrological behaviour of sub-Mediterranean alpine headwater streams in a badlands environment, *J. Hydrol.*, 339, 130–144, <https://doi.org/10.1016/j.jhydrol.2007.03.004>, 2007.
- 895 Davidson, E. A. and Trumbore, S. E.: Gas diffusivity and production of CO₂ in deep soils of the eastern Amazon, *Tellus*, 47B, 550–565, <https://doi.org/10.3402/tellusb.v47i5.16071>, 1995.
- Draix-Bléone Observatory: Observatoire hydrosédimentaire de montagne Draix-Bléone [Data set], Irstea, <https://doi.org/10.17180/obs.draix>, 2015.
- Esteves, M., Descroix, L., Mathys, N., and Marc Lapetite, J.: Soil hydraulic properties in a marly gully catchment (Draix,
900 France), *Catena*, 63, 282–298, <https://doi.org/10.1016/j.catena.2005.06.006>, 2005.
- Fischer, C. and Gaupp, R.: Change of black shale organic material surface area during oxidative weathering: Implications for rock-water surface evolution, *Geochim. Cosmochim. Acta*, 69, 1213–1224, <https://doi.org/10.1016/j.gca.2004.09.021>, 2005.
- Gaillardet, J., Dupré, B., Louvat, P., and Allègre, C. J.: Global silicate weathering and CO₂ consumption rates deduced from the chemistry of large rivers, *Chem. Geol.*, 159, 3–30, [https://doi.org/10.1016/S0009-2541\(99\)00031-5](https://doi.org/10.1016/S0009-2541(99)00031-5), 1999.
- 905 Gaillardet, J., Braud, I., Hankard, F., Anquetin, S., Bour, O., and N. Dorfliger, J. R.: OZCAR: The French Network of Critical Zone Observatories, *Vadose Zo. J.*, 17, 180067, <https://doi.org/10.2136/vzj2018.04.0067>, 2018.

- Garel, E., Marc, V., Ruy, S., Cognard-Plancq, A.-L., Klotz, S., Emblanch, C., and Simler, R.: Large scale rainfall simulation to investigate infiltration processes in a small landslide under dry initial conditions: the Draix hillslope experiment, *Hydrol. Process.*, 26, 2171–2186, <https://doi.org/10.1002/hyp.9273>, 2012.
- 910 Garnett, M. H. and Murray, C.: Processing of CO₂ Samples Collected Using Zeolite Molecular Sieve for ¹⁴C Analysis at the NERC Radiocarbon Facility (East Kilbride, UK), *Radiocarbon*, 55, 410–415, <https://doi.org/10.1017/S0033822200057532>, 2013.
- Garnett, M. H., Newton, J.-A., and Ascough, P. L.: Advances in the Radiocarbon Analysis of Carbon dioxide at the NERC Radiocarbon Facility (East Kilbride) using Molecular sieve Cartridges, *Radiocarbon*, 61, 1855–1865, 915 <https://doi.org/10.1017/RDC.2019.86>, 2019.
- Graz, Y., Di-Giovanni, C., Copard, Y., Elie, M., Faure, P., Laggoun Defarge, F., Lévêque, J., Michels, R., and Olivier, J. E.: Occurrence of fossil organic matter in modern environments: Optical, geochemical and isotopic evidence, *Appl. Geochemistry*, 26, 1302–1314, <https://doi.org/10.1016/j.apgeochem.2011.05.004>, 2011.
- Graz, Y., Di-Giovanni, C., Copard, Y., Mathys, N., Cras, A., and Marc, V.: Annual fossil organic carbon delivery due to 920 mechanical and chemical weathering of marly badlands areas, *Earth Surf. Process. Landforms*, 37, 1263–1271, <https://doi.org/10.1002/esp.3232>, 2012.
- Gu, X., Rempe, D. M., Dietrich, W. E., West, A. J., Lin, T.-C., Jin, L., and Brantley, S. L.: Chemical reactions, porosity, and microfracturing in shale during weathering: The effect of erosion rate, *Geochim. Cosmochim. Acta*, 269, 63–100, <https://doi.org/10.1016/j.gca.2019.09.044>, 2020a.
- 925 Gu, X., Heaney, P. J., Reis, F. D. A. A., and Brantley, S. L.: Deep abiotic weathering of pyrite, *Science* (80-.), 370, eabb8092, <https://doi.org/10.1126/science.abb8092>, 2020b.
- Hardie, S. M. L., Garnett, M. H., Fallick, A. E., Rowland, A. P., and Ostle, N. J.: Carbon Dioxide Capture Using a Zeolite Molecular Sieve Sampling System for Isotopic Studies (¹³C and ¹⁴C) of Respiration, *Radiocarbon*, 47, 441–451, <https://doi.org/10.1017/S0033822200035220>, 2005.
- 930 Hartmann, J. and Moosdorf, N.: The new global lithological map database GLiM: A representation of rock properties at the Earth surface, *Geochemistry, Geophys. Geosystems*, 13, Q12004, <https://doi.org/10.1029/2012GC004370>, 2012.
- Hashimoto, S. and Komatsu, H.: Relationships between soil CO₂ concentration and CO₂ production, temperature, water content, and gas diffusivity: implications for field studies through sensitivity analyses, *J. For. Res.*, 11, 41–50, <https://doi.org/10.1007/s10310-005-0185-4>, 2006.
- 935 Heimsath, A. M., DiBiase, R. A., and Whipple, K. X.: Soil production limits and the transition to bedrock-dominated landscapes, *Nat. Geosci.*, 5, 210–214, <https://doi.org/10.1038/ngeo1380>, 2012.
- Hemingway, J. D., Hilton, R. G., Hovius, N., Eglinton, T. I., Haghipour, N., Wacker, L., Chen, M.-C., and Galy, V. V.: Microbial oxidation of lithospheric organic carbon in rapidly eroding tropical mountain soils, *Science* (80-.), 360, 209–212, <https://doi.org/10.1126/science.aao6463>, 2018.
- 940 Hicks Pries, C., Angert, A., Castanha, C., Hilman, B., and Torn, M. S.: Using respiration quotients to track changing sources

- of soil respiration seasonally and with experimental warming, *Biogeosciences*, 17, 3045–3055, <https://doi.org/10.5194/bg-17-3045-2020>, 2020.
- Hilton, R. G. and West, A. J.: Mountains, erosion and the carbon cycle, *Nat. Rev. Earth Environ.*, 1, 284–299, <https://doi.org/10.1038/s43017-020-0058-6>, 2020.
- 945 Hilton, R. G., Turowski, J. M., Winnick, M., Dellinger, M., Schleppei, P., Williams, K. H., Lawrence, C. R., Maher, K., West, M., and Hayton, A.: Concentration-Discharge Relationships of Dissolved Rhenium in Alpine Catchments Reveal Its Use as a Tracer of Oxidative Weathering, *Water Resour. Res.*, 57, e2021WR029844, <https://doi.org/10.1029/2021WR029844>, 2021.
- Janjou, D.: Descriptif des cartes géologiques à 1/50 000 format “vecteurs” [Map], *Bur. Rech. géologiques minières, Fr.*, RP-53571, 2004.
- 950 Kalks, F., Noren, G., Mueller, C. W., Helfrich, M., Rethemeyer, J., and Don, A.: Geogenic organic carbon in terrestrial sediments and its contribution to total soil carbon, *SOIL*, 347–362, <https://doi.org/10.5194/soil-7-347-2021>, 2021.
- Keller, C. K. and Bacon, D. H.: Soil respiration and georespiration distinguished by transport analyses of vadose CO₂, 13CO₂, and 14CO₂, *Global Biogeochem. Cycles*, 12, 361–372, <https://doi.org/10.1029/98GB00742>, 1998.
- Killops, S. and Killops, V.: *Introduction to Organic Geochemistry*, 2nd ed., Blackwell Science Publishing, Malden, USA, 955 393 pp., 2005.
- Klotz, S., Le Bouteiller, C., Mathys, N., Fontaine, F., Ravanat, X., Olivier, J.-E., Liébault, F., Jantzi, H., Coulmeau, P., Richard, D., Cambon, J.-P., and Meunier, M.: A high-frequency, long-term data set of hydrology and sediment yield: The alpine badland catchments of Draix-Bléone Observatory, *Earth Syst. Sci. Data Discuss.*, 2023, 1–26, <https://doi.org/10.5194/essd-2023-34>, 2023.
- 960 Lebedeva, M. I. and Brantley, S. L.: Relating the depth of the water table to the depth of weathering, *Earth Surf. Process. Landforms*, 45, 2167–2178, <https://doi.org/10.1002/esp.4873>, 2020.
- Lefèvre, R., Barré, P., Moyano, F. E., Christensen, B. T., Bardoux, G., Eglin, T., Girardin, C., Houot, S., Kätterer, T., van Oort, F., and Chenu, C.: Higher temperature sensitivity for stable than for labile soil organic carbon - Evidence from incubations of long-term bare fallow soils, *Glob. Chang. Biol.*, 20, 633–640, <https://doi.org/10.1111/gcb.12402>, 2014.
- 965 Li, S.-L., Calmels, D., Han, G., Gaillardet, J., and Liu, C.-Q.: Sulfuric acid as an agent of carbonate weathering constrained by $\delta^{13}\text{CDIC}$: Examples from Southwest China, *Earth Planet. Sci. Lett.*, 270, 189–199, <https://doi.org/10.1016/j.epsl.2008.02.039>, 2008.
- Liang, L. L., Riveros-Iregui, D. A., Emanuel, R. E., and McGlynn, B. L.: A simple framework to estimate distributed soil temperature from discrete air temperature measurements in data-scarce regions, *J. Geophys. Res. Atmos.*, 119, 407–417, 970 <https://doi.org/10.1002/2013JD020597>, 2014.
- Lofi, J., Pezard, P., Loggia, D., Garel, E., Gautier, S., Merry, C., and Bondabou, K.: Geological discontinuities, main flow path and chemical alteration in a marly hill prone to slope instability: Assessment from petrophysical measurements and borehole image analysis, *Hydrol. Process.*, 26, 2071–2084, <https://doi.org/10.1002/hyp.7997>, 2012.
- Longbottom, T. L. and Hockaday, W. C.: Molecular and isotopic composition of modern soils derived from kerogen-rich

- 975 bedrock and implications for the global C cycle, *Biogeochemistry*, 143, 239–255, <https://doi.org/10.1007/s10533-019-00559-4>, 2019.
- Maier, M. and Schack-Kirchner, H.: Using the gradient method to determine soil gas flux: A review, *Agric. For. Meteorol.*, 192–193, 78–95, <https://doi.org/10.1016/j.agrformet.2014.03.006>, 2014.
- Mallet, F., Marc, V., Douvinet, J., Rossello, P., Joly, D., and Ruy, S.: Assessing soil water content variation in a small
980 mountainous catchment over different time scales and land covers using geographical variables, *J. Hydrol.*, 591, 125593, <https://doi.org/10.1016/j.jhydrol.2020.125593>, 2020.
- Maquaire, O., Ritzenthaler, A., Fabre, D., Ambroise, B., Thiery, Y., Truchet, E., Malet, J.-P., and Monnet, J.: Caractérisation des profils de formations superficielles par pénétrométrie dynamique à énergie variable : application aux marnes noires de Draix (Alpes-de-Haute-Provence, France), *Comptes Rendus Geosci.*, 334, 835–841, [https://doi.org/10.1016/S1631-9850713\(02\)01788-1](https://doi.org/10.1016/S1631-9850713(02)01788-1), 2002.
- Massman, W. J.: A review of the molecular diffusivities of H₂O, CO₂, CH₄, CO, O₃, SO₂, NH₃, N₂O, NO, and NO₂ in air, O₂ and N₂ near STP, *Atmos. Environ.*, 32, 1111–1127, [https://doi.org/10.1016/S1352-2310\(97\)00391-9](https://doi.org/10.1016/S1352-2310(97)00391-9), 1998.
- Mathys, N. and Klotz, S.: DRAIX: A field laboratory for research on hydrology and erosion in mountain areas, in: *Proceedings of the 4th Canadian Conference on Geohazards: From Causes to Management*, 2008.
- 990 Mathys, N., Brochot, S., Meunier, M., and Richard, D.: Erosion quantification in the small marly experimental catchments of Draix (Alpes de Haute Provence, France). Calibration of the ETC rainfall–runoff–erosion model, *Catena*, 50, 527–548, [https://doi.org/10.1016/S0341-8162\(02\)00122-4](https://doi.org/10.1016/S0341-8162(02)00122-4), 2003.
- Millington, R. J.: Gas Diffusion in Porous Media, *Science* (80-.), 130, 100–102, <https://doi.org/10.1126/science.130.3367.100-a>, 1959.
- 995 Mills, B. J. W., Donnadieu, Y., and Goddérís, Y.: Spatial continuous integration of Phanerozoic global biogeochemistry and climate, *Gondwana Res.*, 100, 73–86, <https://doi.org/10.1016/j.gr.2021.02.011>, 2021.
- Milodowski, D. T., Mudd, S. M., and Mitchard, E. T. A.: Erosion rates as a potential bottom-up control of forest structural characteristics in the Sierra Nevada Mountains, *Ecology*, 96, 31–38, <https://doi.org/10.1890/14-0649.1>, 2015.
- Moon, S., Chamberlain, C. P., and Hilley, G. E.: New estimates of silicate weathering rates and their uncertainties in global
1000 rivers, *Geochim. Cosmochim. Acta*, 134, 257–274, <https://doi.org/10.1016/j.gca.2014.02.033>, 2014.
- Oertel, C., Matschullat, J., Zurba, K., Zimmermann, F., and Erasmi, S.: Greenhouse gas emissions from soils—A review, *Geochemistry*, 76, 327–352, <https://doi.org/10.1016/j.chemer.2016.04.002>, 2016.
- Oostwoud Wijdenes, D. J. and Ergenzinger, P.: Erosion and sediment transport on steep marly hillslopes, Draix, Haute-Provence, France: an experimental field study, *Catena*, 33, 179–200, [https://doi.org/10.1016/S0341-8162\(98\)00076-9](https://doi.org/10.1016/S0341-8162(98)00076-9), 1998.
- 1005 Peng, S., Hu, Q., and Hamamoto, S.: Diffusivity of rocks: Gas diffusion measurements and correlation to porosity and pore size distribution, *Water Resour. Res.*, 48, W02507, <https://doi.org/10.1029/2011WR011098>, 2012.
- Penman, H. L.: Gas and vapour movements in the soil: I. The diffusion of vapours through porous solids, *J. Agric. Sci.*, 30, 437–462, <https://doi.org/10.1017/S0021859600048164>, 1940.

- Petsch, S. T.: Weathering of Organic Carbon, in: *Treatise on Geochemistry*, vol. 12, Elsevier, Amsterdam, Netherlands, 217–238, <https://doi.org/10.1016/B978-0-08-095975-7.01013-5>, 2014.
- 1010 Pirk, N., Mastepanov, M., Parmentier, F.-J. W., Lund, M., Crill, P., and Christensen, T. R.: Calculations of automatic chamber flux measurements of methane and carbon dioxide using short time series of concentrations, *Biogeosciences*, 13, 903–912, <https://doi.org/10.5194/bg-13-903-2016>, 2016.
- Rovéra, G. and Robert, Y.: Conditions climatiques hivernales et processus d'érosion périglaciaires dans les bad-lands marneux de Draix (800 m, Alpes du Sud, France), *Géographie Phys. Quat.*, 59, 31–48, <https://doi.org/10.7202/013735ar>, 2006.
- Roylands, T., Hilton, R. G., Garnett, M. H., Soulet, G., Newton, J.-A., Peterkin, J. L., and Hancock, P.: Capturing the short-term variability of carbon dioxide emissions from sedimentary rock weathering in a remote mountainous catchment, New Zealand, *Chem. Geol.*, 608, 121024, <https://doi.org/10.1016/j.chemgeo.2022.121024>, 2022.
- 1020 Sánchez-Cañete, E. P., Barron-Gafford, G. A., and Chorover, J.: A considerable fraction of soil-respired CO₂ is not emitted directly to the atmosphere, *Sci. Rep.*, 8, 13518, <https://doi.org/10.1038/s41598-018-29803-x>, 2018.
- Seifert, A.-G., Trumbore, S., Xu, X., Zhang, D., Kothe, E., and Gleixner, G.: Variable effects of labile carbon on the carbon use of different microbial groups in black slate degradation, *Geochim. Cosmochim. Acta*, 75, 2557–2570, <https://doi.org/10.1016/j.gca.2011.02.037>, 2011.
- 1025 Soucémarianadin, L. N., Cécillon, L., Guenet, B., Chenu, C., Baudin, F., Nicolas, M., Girardin, C., and Barré, P.: Environmental factors controlling soil organic carbon stability in French forest soils, *Plant Soil*, 426, 267–286, <https://doi.org/10.1007/s11104-018-3613-x>, 2018.
- Soulet, G., Hilton, R. G., Garnett, M. H., Dellinger, M., Croissant, T., Ogrič, M., and Klotz, S.: Technical note: In situ measurement of flux and isotopic composition of CO₂ released during oxidative weathering of sedimentary rocks, *Biogeosciences*, 15, 4087–4102, <https://doi.org/10.5194/bg-15-4087-2018>, 2018.
- 1030 Soulet, G., Hilton, R. G., Garnett, M. H., Roylands, T., Klotz, S., Croissant, T., Dellinger, M., and Le Bouteiller, C.: Temperature control on CO₂ emissions from the weathering of sedimentary rocks, *Nat. Geosci.*, 14, 665–671, <https://doi.org/10.1038/s41561-021-00805-1>, 2021.
- Stolper, D. A., Bender, M. L., Dreyfus, G. B., Yan, Y., and Higgins, J. A.: A Pleistocene ice core record of atmospheric O₂ concentrations, *Science (80-.)*, 353, 1427–1430, <https://doi.org/10.1126/science.aaf5445>, 2016.
- 1035 Sullivan, P. L., Hynek, S. A., Gu, X., Singha, K., White, T., West, N., Kim, H., Clarke, B., Kirby, E., Duffy, C., and Brantley, S. L.: Oxidative dissolution under the channel leads geomorphological evolution at the Shale Hills catchment, *Am. J. Sci.*, 316, 981–1026, <https://doi.org/10.2475/10.2016.02>, 2016.
- Sundquist, E. T. and Visser, K.: The Geologic History of the Carbon Cycle, in: *Treatise on Geochemistry*, vol. 8, Elsevier, Amsterdam, Netherlands, 425–472, <https://doi.org/10.1016/B0-08-043751-6/08133-0>, 2003.
- 1040 Tamamura, S., Ueno, A., Aramaki, N., Matsumoto, H., Uchida, K., Igarashi, T., and Kaneko, K.: Effects of oxidative weathering on the composition of organic matter in coal and sedimentary rock, *Org. Geochem.*, 81, 8–19,

- <https://doi.org/10.1016/j.orggeochem.2015.01.006>, 2015.
- 1045 Tokunaga, T. K., Kim, Y., Conrad, M. E., Bill, M., Hobson, C., Williams, K. H., Dong, W., Wan, J., Robbins, M. J., Long, P. E., Faybishenko, B., Christensen, J. N., and Hubbard, S. S.: Deep Vadose Zone Respiration Contributions to Carbon Dioxide Fluxes from a Semiarid Floodplain, *Vadose Zo. J.*, 15, vzt2016.02.0014, <https://doi.org/10.2136/vzt2016.02.0014>, 2016.
- Torres, M. A., West, A. J., and Li, G.: Sulphide oxidation and carbonate dissolution as a source of CO₂ over geological timescales, *Nature*, 507, 346–349, <https://doi.org/10.1038/nature13030>, 2014.
- 1050 Travelletti, J., Sailhac, P., Malet, J.-P., Grandjean, G., and Ponton, J.: Hydrological response of weathered clay-shale slopes: water infiltration monitoring with time-lapse electrical resistivity tomography, *Hydrol. Process.*, 26, 2106–2119, <https://doi.org/10.1002/hyp.7983>, 2012.
- Tune, A. K., Druhan, J. L., Wang, J., Bennett, P. C., and Rempe, D. M.: Carbon Dioxide Production in Bedrock Beneath Soils Substantially Contributes to Forest Carbon Cycling, *J. Geophys. Res. Biogeosciences*, 125, e2020JG005795, 1055 <https://doi.org/10.1029/2020JG005795>, 2020.
- Tune, A. K., Druhan, J. L., Lawrence, C. R., and Rempe, D. M.: Deep root activity overprints weathering of petrogenic organic carbon in shale, *Earth Planet. Sci. Lett.*, 607, 118048, <https://doi.org/10.1016/j.epsl.2023.118048>, 2023.
- Wan, J., Tokunaga, T. K., Brown, W., Newman, A. W., Dong, W., Bill, M., Beutler, C. A., Henderson, A. N., Harvey-Costello, N., Conrad, M. E., Bouskill, N. J., Hubbard, S. S., and Williams, K. H.: Bedrock weathering contributes to 1060 subsurface reactive nitrogen and nitrous oxide emissions, *Nat. Geosci.*, 14, 217–224, <https://doi.org/10.1038/s41561-021-00717-0>, 2021.
- Weisbrod, N., Dragila, M. I., Nachshon, U., and Pillersdorf, M.: Falling through the cracks: The role of fractures in Earth-atmosphere gas exchange, *Geophys. Res. Lett.*, 36, L02401, <https://doi.org/10.1029/2008GL036096>, 2009.
- White, A. F. and Brantley, S. L.: The effect of time on the weathering of silicate minerals: why do weathering rates differ in 1065 the laboratory and field?, *Chem. Geol.*, 202, 479–506, <https://doi.org/10.1016/j.chemgeo.2003.03.001>, 2003.
- Włodarczyk, A., Lirski, M., Fogtman, A., Koblowska, M., Bidziński, G., and Matlakowska, R.: The Oxidative Metabolism of Fossil Hydrocarbons and Sulfide Minerals by the Lithobiontic Microbial Community Inhabiting Deep Subterrestrial Kupferschiefer Black Shale, *Front. Microbiol.*, 9, 972, <https://doi.org/10.3389/fmicb.2018.00972>, 2018.
- Yan, Y., Brook, E. J., Kurbatov, A. V., Severinghaus, J. P., and Higgins, J. A.: Ice core evidence for atmospheric oxygen 1070 decline since the Mid-Pleistocene transition, *Sci. Adv.*, 7, eabj9341, <https://doi.org/10.1126/sciadv.abj9341>, 2021.